



University of Tehran
Faculty of Engineering
School of Electrical and Computer Engineering



Introduction to cognitive science

Homework 2 – Phase 1

Parsa Daghigh
810101419

Spring 2025

Figures

Figure 1- Histogram of the recorded voltage amplitudes for the entire dataset	4
Figure 2- Amplitude against time	4
Figure 3- Unfiltered data and the data after applying the filter.....	5
Figure 4- Waveform for every detected spike	5
Figure 5- Num of PCs and their power	6
Figure 6 - Plot of PCA.....	6
Figure 7 - Elbow curve and Silhouette Analysis.....	7
Figure 8 - K-Means clustering	7
Figure 9- Checking spike sorting with first threshold	8
Figure 10 - Checking spike sorting with new threshold	8
Figure 11 - Checking spike sorting with custom formula	9
Figure 12 - Determining K for tSNE analysis	9
Figure 13 - tSNE embedding with K = 2.....	10
Figure 14 - Histogram of ross-data	11
Figure 15 - PCA of ROSS with t-dist.....	11
Figure 16 - PCA of ROSS with kmeans	11
Figure 17 - t-dist waveform.....	12
Figure 18 - kmeans waveform	12
Figure 19 - Noises detected doing denoise	12
Figure 20 - Plot of PCA classes after resorting one cluster	13
Figure 21 - Each cluster waveforms.....	13
Figure 22 - 3D plot of two clustered after merge.....	14
Figure 23 – Raw data spike detection zoomed	14
Figure 24 – Raw data spike detection with different clusters	14
Figure 25 - Raster plot of neuron 64	15
Figure 26 - PSTH is sufficient statistic for Poission with rate λ	17
Figure 27 - Smoothed Fano Factor for different neurons	18
Figure 28 - MMFF of four categories	19
Figure 29 - Multiclass SVM for given sliding window.....	20
Figure 30 - Time-Time decoding barplot	21
Figure 31 - Mutual Information for Neuron 60.....	22
Figure 32 - Mutual Information for 0-9 Neurons.....	23
Figure 33 - d-prime analysis	24
Figure 34- d-prime analysis for 0-9 Neurons.....	24
Figure 35 - RDM and Kendall Tau correlation.....	25
Figure 36 - GLM result of different time points	26
Figure 37 - GLM for RDM.....	27
Figure 38 - PAC plot with Canolty and MI method for different categories	28
Figure 39 - PSD for neuron 0.....	29
Figure 40 - PAC with Canolty and MI method for neuron 0 and 1	29

Abstract

This project began by developing a full spike-sorting pipeline on a single-channel extracellular recording sampled at 30 kHz. We first applied a seventh-order Butterworth band-pass filter (300–3000 Hz) to isolate action-potential signals from low-frequency local field potentials and high-frequency noise. Spikes were detected using a data-driven threshold ($\theta = 5\sigma_n$), and both negative and positive deflections were captured. Each detected event was windowed (± 2 ms) and described by its waveform, after which principal component analysis reduced dimensionality to the three most informative components. K-means clustering—guided by t-SNE visualizations—segregated these features into putative single-unit spikes, and performance was quantitatively assessed against ground-truth spike times, revealing trade-offs in precision and recall under different threshold schemes.

In the second phase, we turned to a large IT-cortex dataset comprising 92 neurons recorded over 5000 trials, each trial presenting one of 500 images from four semantic categories (face, body, natural, artificial). Peri-stimulus time histograms showed that face stimuli elicited the strongest and most rapid firing-rate increase, peaking around 120–160 ms. Fano-factor analysis demonstrated a quenching of trial-to-trial variability during stimulus processing, with subtle category differences. Complementary measures—mutual information and d' —also peaked in this window, confirming that category-selective information emerges in IT around 150–180 ms.

Finally, we examined the representational geometry of the IT population via representational dissimilarity matrices (RDMs). By computing Kendall's τ correlation between neural RDMs (Euclidean distances among all 500 stimulus-evoked population patterns) and a binary ground-truth RDM (same vs. different category), we found maximal alignment at ~ 180 ms, dovetailing with the PSTH, decoding, and information-theoretic analyses. A univariate GLM regressing the categorical RDM on neural dissimilarities yielded low explained variance, indicating that while IT activity does reflect category structure, it does so modestly at the population level. Across these phases, the project illustrates a comprehensive pipeline—from raw signal processing through spike sorting to high-level cognitive decoding—tracing the emergence of object-category representations in the primate visual system.

Question 1 – Spike Sorting from Scratch

1.1 Filtering data

The raw signal, sampled at 30 kHz, contained both low-frequency local field potentials and high-frequency noise, so our first step was to isolate the frequency band where spikes typically occur. We applied a band-pass filter with cutoffs at 300 Hz and 3000 Hz. This effectively preserved the components most likely to contain spike events, while attenuating both low-frequency drift and high-frequency artifacts.

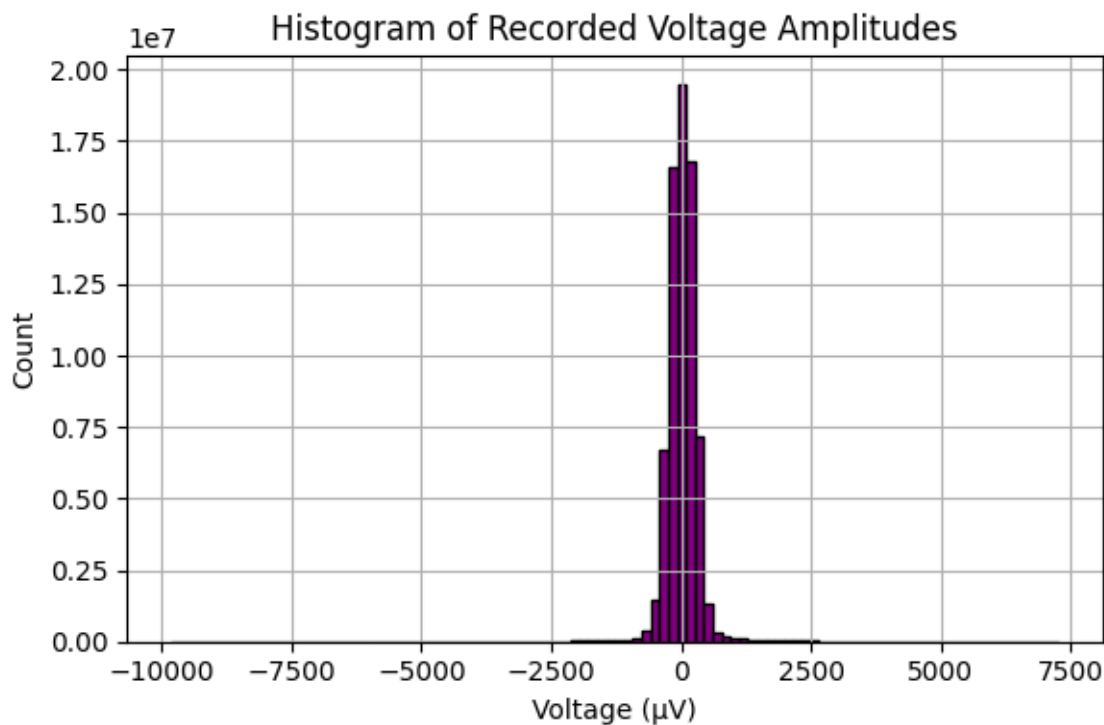


Figure 1- Histogram of the recorded voltage amplitudes for the entire dataset

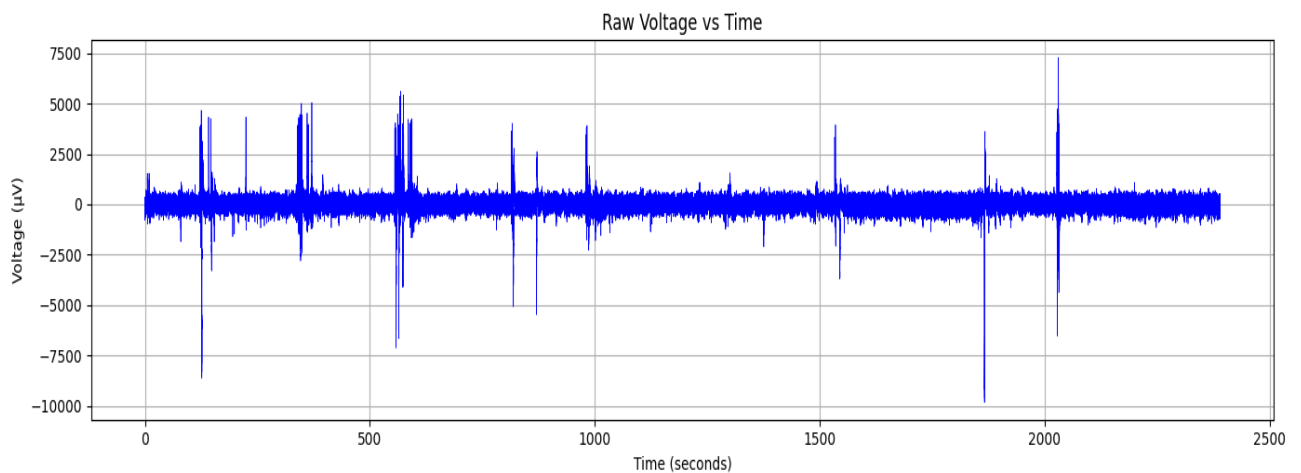


Figure 2- Amplitude against time

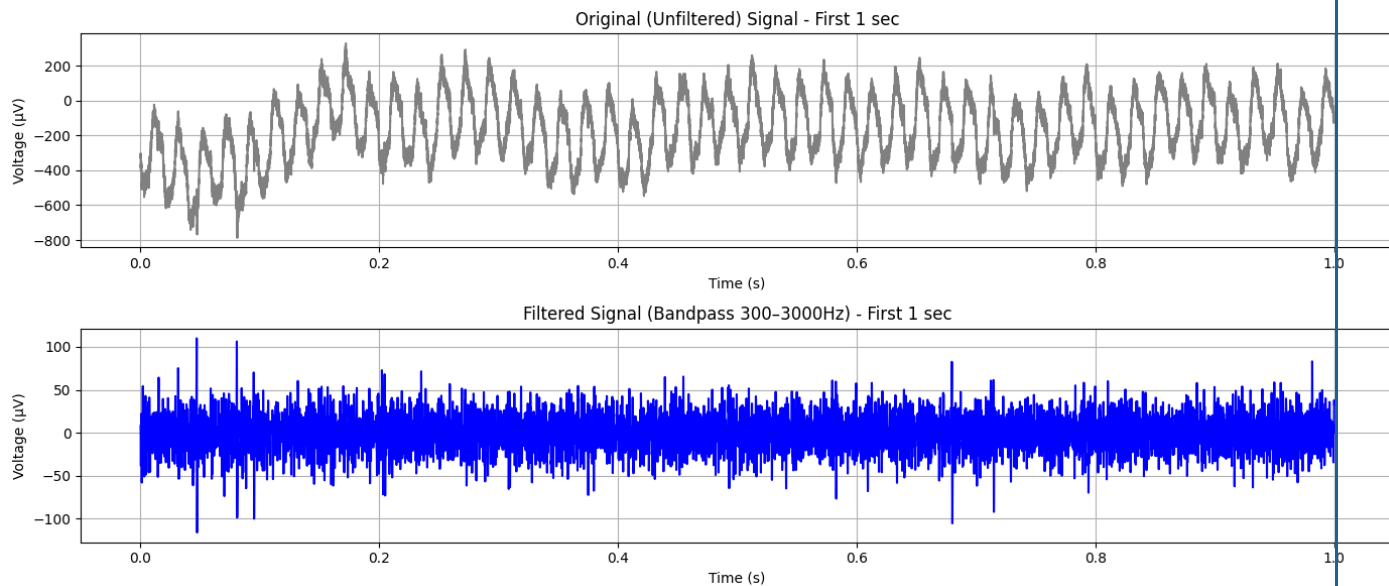


Figure 3- Unfiltered data and the data after applying the filter

1.2 Detecting spikes

Spike detection was performed using a threshold-based approach. We estimated the background noise level using the median absolute deviation (MAD) and set the threshold at five times this noise estimate, resulting in a threshold of approximately $\theta = 104.11 \mu\text{V}$. Spikes were identified as either **negative or positive peaks** exceeding this threshold. A total of **29,031 negative** and **16,405 positive** peaks were detected, yielding **45,436 candidate spikes** in total. Each spike was extracted as a waveform consisting of 121 samples (± 2 ms at 30 kHz), resulting in a dataset of 45,436 waveforms for subsequent analysis.

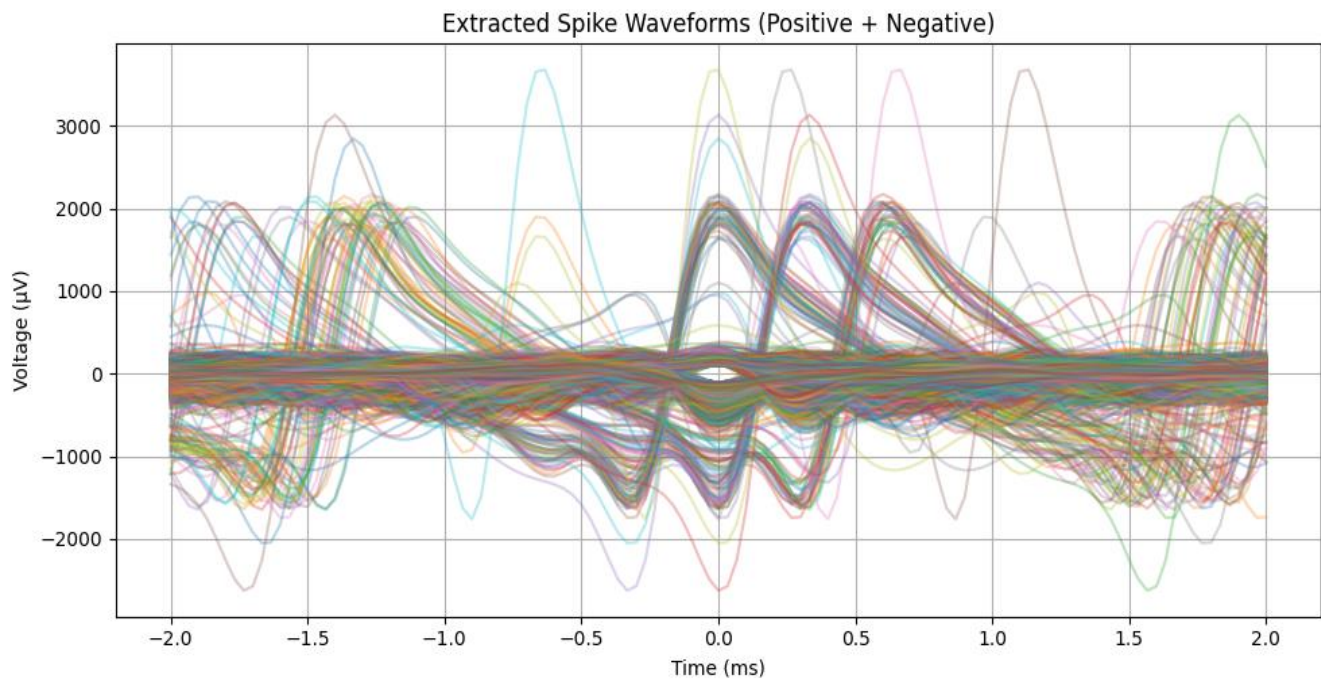


Figure 4- Waveform for every detected spike

For each detected spike, we extracted a fixed-length segment of the signal surrounding the peak—specifically, a window of 4 milliseconds (± 2 ms) centered on the spike. These

segments formed a matrix of waveforms, each one representing a single candidate spike event.

1.3 PCA and Clustering

To reduce dimensionality and retain the most informative features of the spike shapes, we applied Principal Component Analysis (PCA) to the waveform matrix. The first three principal components explained **63.1% of the total variance**, providing a compact and effective representation of the data for clustering.

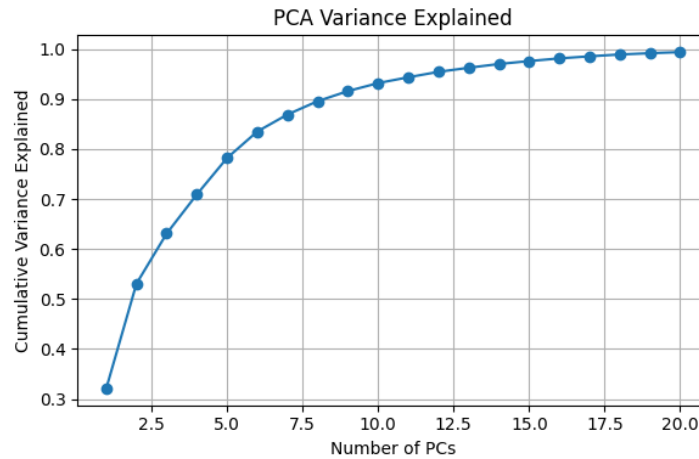


Figure 5- Num of PCs and their power

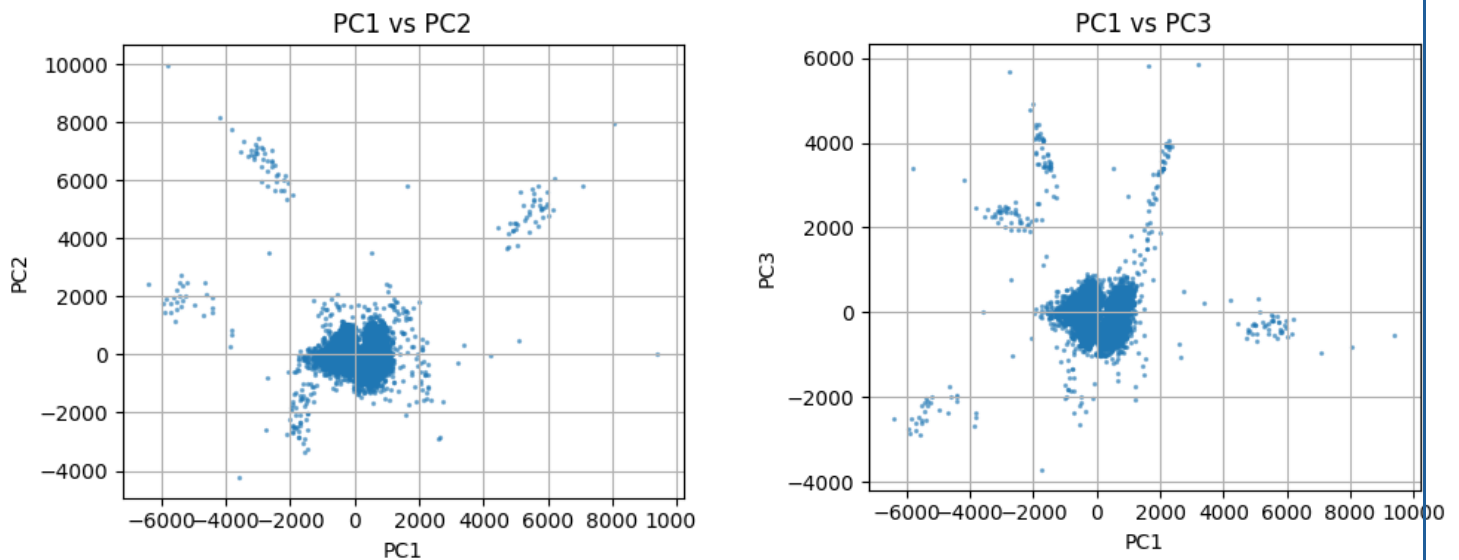


Figure 6 - Plot of PCA

We then applied **k-means clustering with $K = 3$** , selected based on t-SNE visualization and qualitative assessment of the PCA scatter plot. This clustering yielded three distinct groups of waveforms, each interpreted as representing a different putative neuron or noise component. Cluster quality was further evaluated by examining the average waveform shape within each

cluster, allowing for interpretation of waveform consistency and potential overlap.

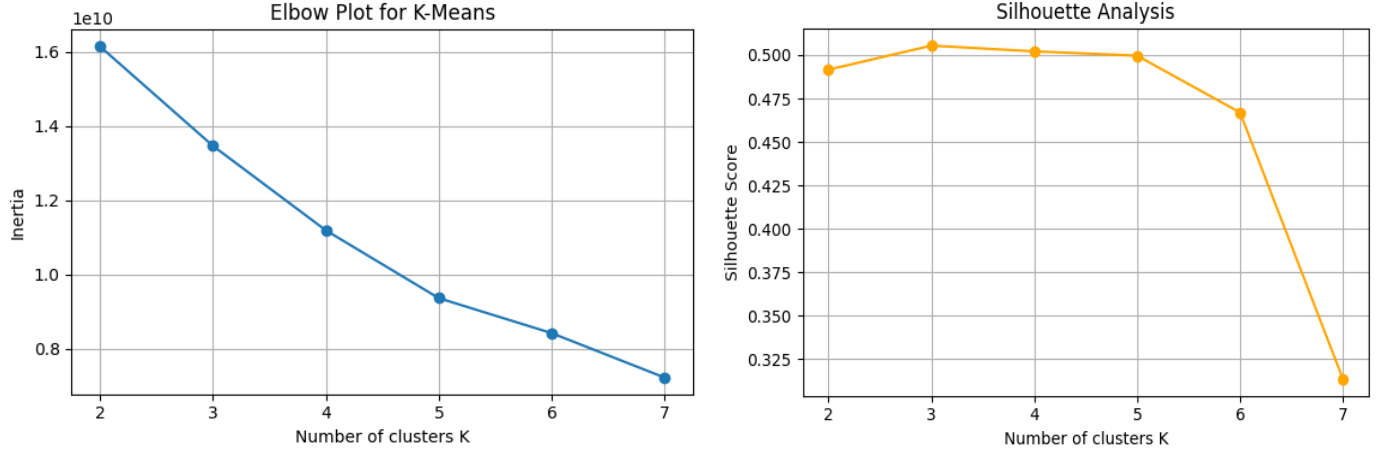


Figure 7 - Elbow curve and Silhouette Analysis

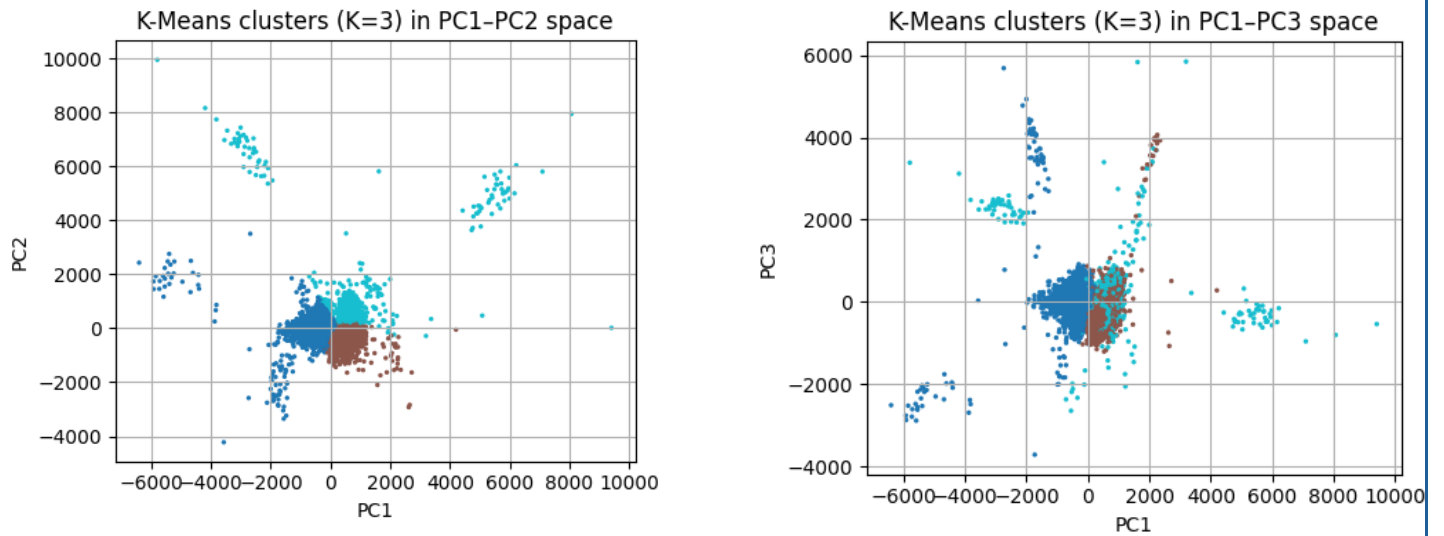


Figure 8 - K-Means clustering

1.3 Changing threshold and checking with Spikes.mat

To assess whether using the alternative threshold θ_{new} improved the spike-sorting results, we implemented both detection schemes and compared their effectiveness in identifying true spikes within the relevant evaluation window. The original threshold, defined as $\theta = 5\sigma_n$, was based on the median absolute deviation and aimed to ensure high specificity by avoiding false positives. However, this approach resulted in extremely few detected spikes—sometimes fewer than five—in the ground truth region, indicating that the threshold was too conservative. We then applied the alternative θ_{new} formula as specified in the assignment, which scaled the detection threshold relative to the maximum observed amplitude. While this was more lenient in principle, the actual maximum amplitude in the signal was still high enough that the resulting θ_{new} remained too strict. The number of detected spikes remained far below the expected range, and performance metrics such as precision, recall, and F1-score were effectively zero.

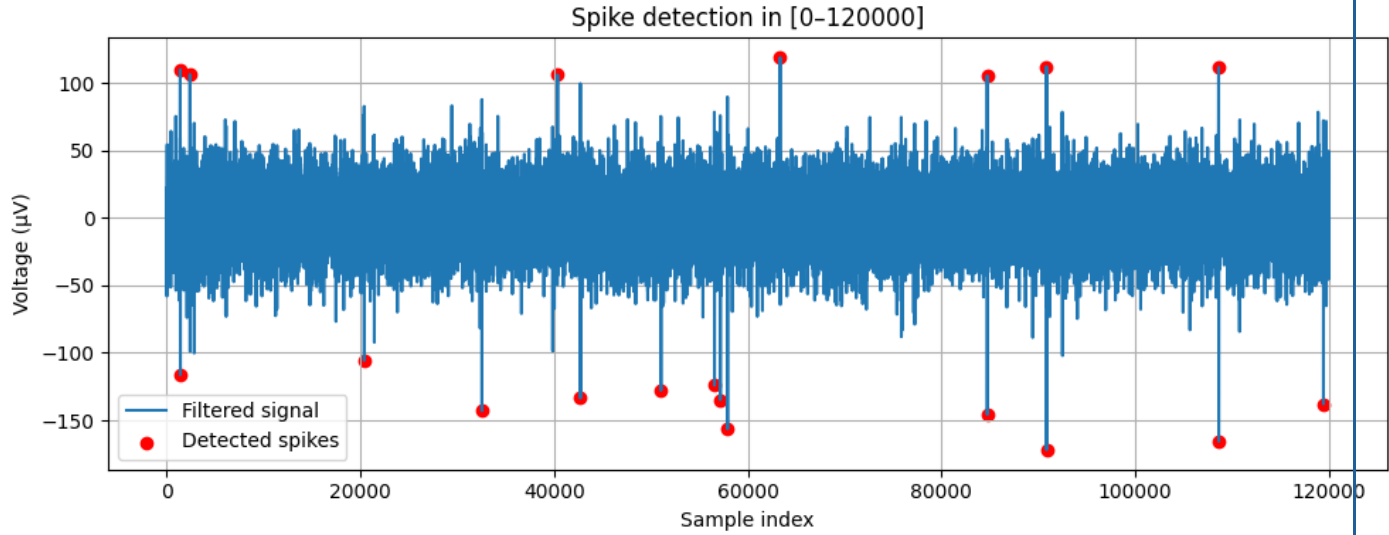


Figure 9- Checking spike sorting with first threshold

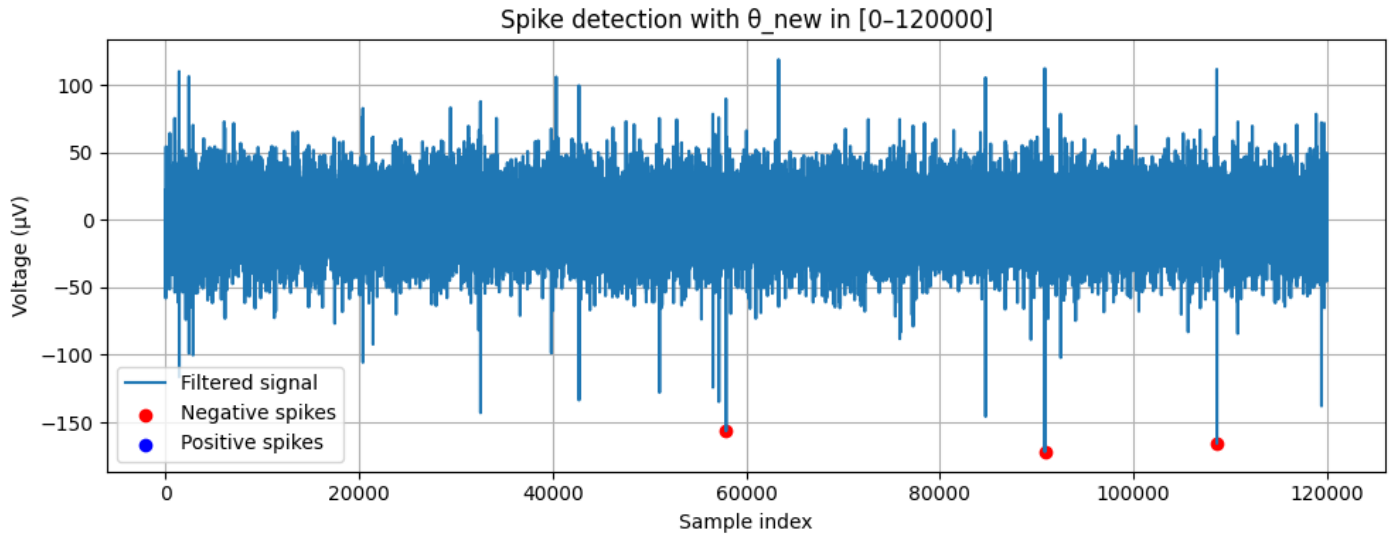


Figure 10 - Checking spike sorting with new threshold

We concluded that neither of the originally prescribed thresholds was well-suited for this dataset. A more effective strategy involved empirically tuning the threshold by lowering the noise multiplier from 5 to 3 in the original MAD-based formula. This allowed for better sensitivity while still avoiding most noise. Therefore, although θ_{new} aimed to adapt to the signal's scale, it did not improve spike detection in practice, and a carefully calibrated, noise-driven threshold (e.g., $3 \times \sigma_n$) provided more meaningful results.

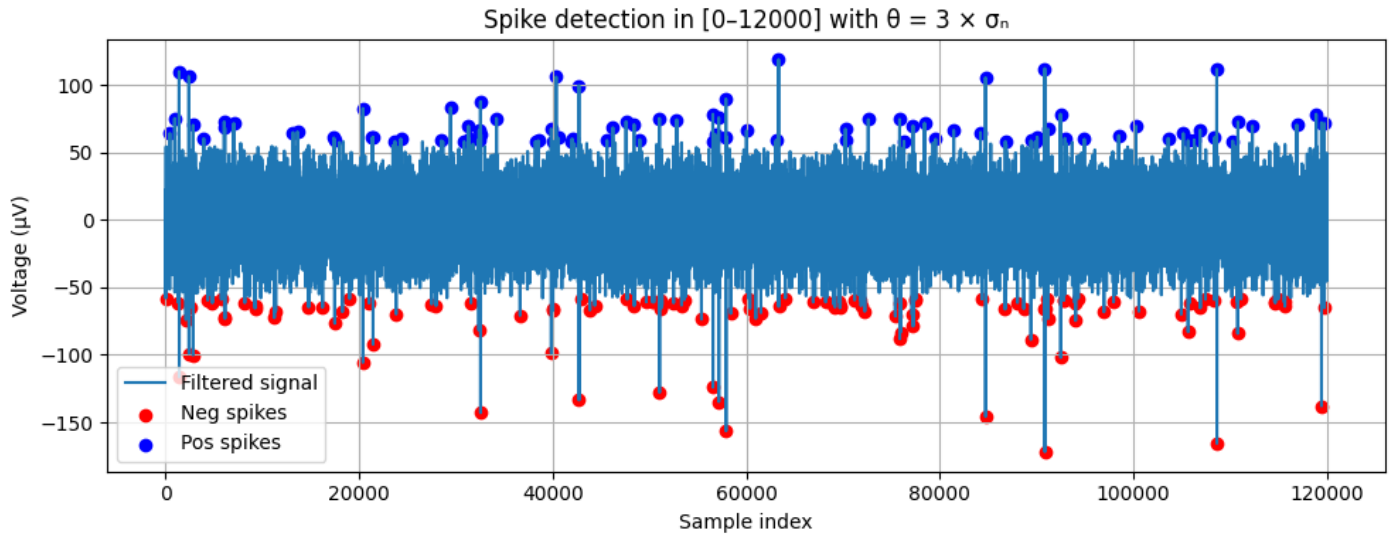


Figure 11 - Checking spike sorting with custom formula

1.4 Using tSNE instead of PCA

To further evaluate the separability of detected spike waveforms, we applied **t-distributed Stochastic Neighbor Embedding (t-SNE)** as a non-linear dimensionality reduction technique. Unlike PCA, which projects data linearly and captures variance globally, t-SNE is particularly effective at revealing local structure and potential clustering in high-dimensional data—an advantage when analyzing complex, overlapping spike waveforms. We applied t-SNE to a subset of 10,000 extracted waveforms using the default perplexity and a learning rate tuned for stability. The algorithm computed nearest neighbors, conditional probabilities, and ultimately converged with a KL divergence of approximately 1.61 after 1,000 iterations, indicating a stable low-dimensional embedding. Based on the resulting 2D t-SNE scatter plot, we observed visually distinct groupings suggestive of at least two major spike populations.

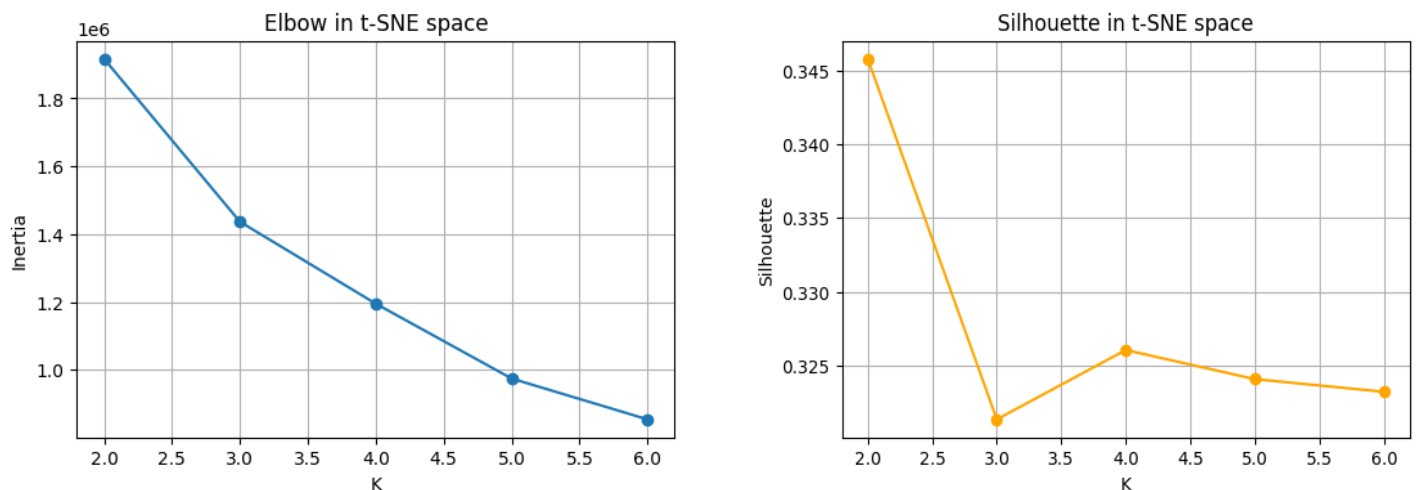


Figure 12 - Determining K for tSNE analysis

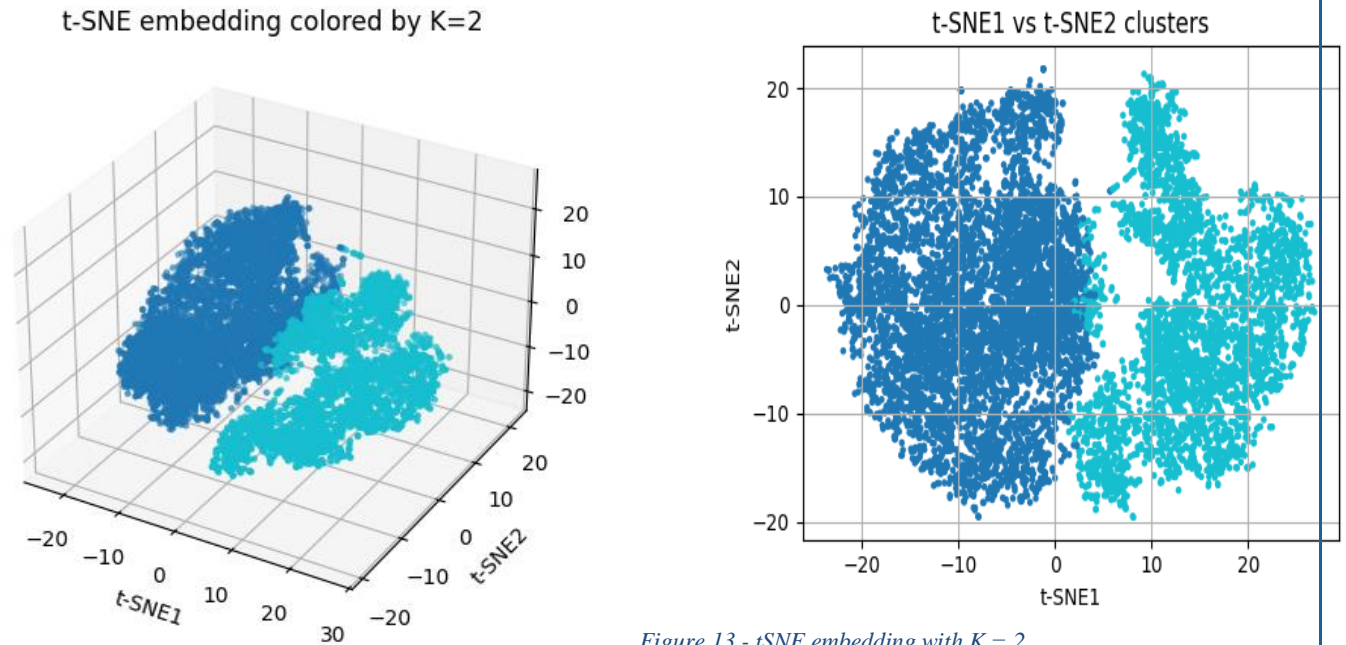


Figure 13 - tSNE embedding with $K = 2$

Question 2 – Spike Sorting using ROSS

In this section, we used the **ROSS (Robust Online Spike Sorting)** toolbox to explore a semi-automated spike-sorting workflow, which includes detection, auto sorting, manual refinement, and visualization. The analysis was conducted using `ross-data.mat`, which contains raw extracellular voltage recordings. ROSS provides a graphical user interface with modular steps, allowing users to interactively control filtering, thresholding, clustering, and refinement operations. Before using the tool, we reviewed its documentation to understand its internal algorithms and adjustable parameters.

2.1 Detection

The first step in the process was **spike detection**. We loaded the raw data and adjusted the bandpass filter to isolate spikes, setting the passband between 300 Hz and 3000 Hz to suppress low-frequency drift and high-frequency noise. The detection threshold was calculated based on the estimated noise level, using the standard deviation of the signal. After adjusting the threshold value to suit the signal's noise characteristics, we initiated the detection by clicking the “Start Detection” button. The software identified spikes that crossed the threshold and visualized them in a PCA plot. This step extracted the spike waveforms and their timestamps, which were saved for downstream clustering.

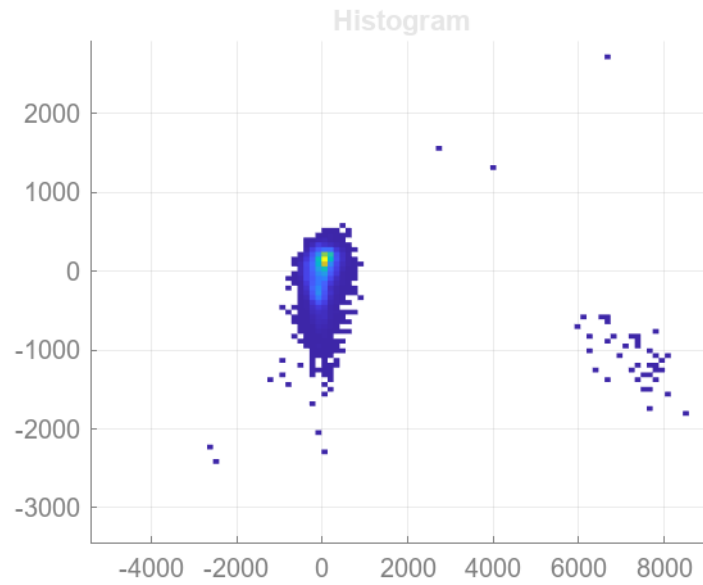


Figure 14 - Histogram of ross-data

2.2 Auto-Sorting

Next, we performed **auto sorting** using ROSS's built-in automatic clustering pipeline. This step applies a combination of t-distribution mixture models, Gaussian Mixture Models (GMM), k-means, and template matching to automatically assign spike waveforms to clusters (presumed neurons). Noise and outliers were removed using statistical filtering, and spike alignment was applied to improve temporal consistency across waveforms. The results were displayed in PCA and waveform plots. Based on the auto-sorting output, we observed that the dataset contained **three distinct clusters**, each likely corresponding to a separate neuron. These clusters were well separated in PCA space, and their average waveforms displayed consistent and distinguishable shapes.

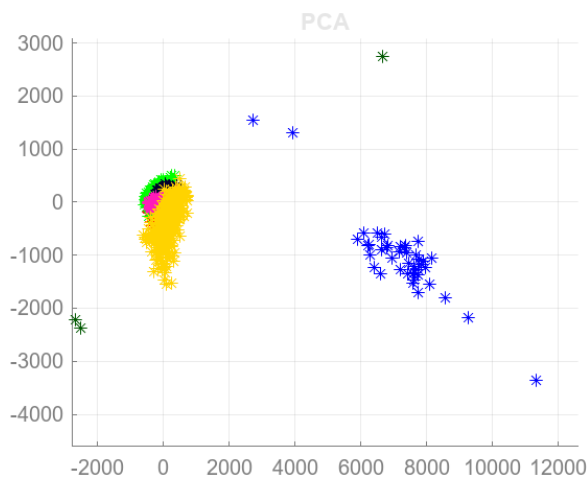


Figure 15 - PCA of ROSS with t-dist

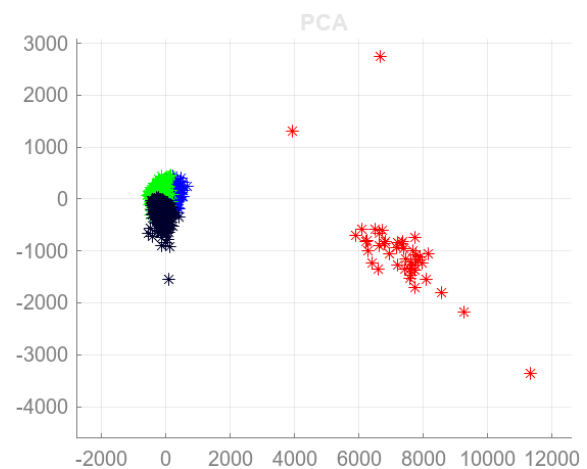


Figure 16 - PCA of ROSS with kmeans

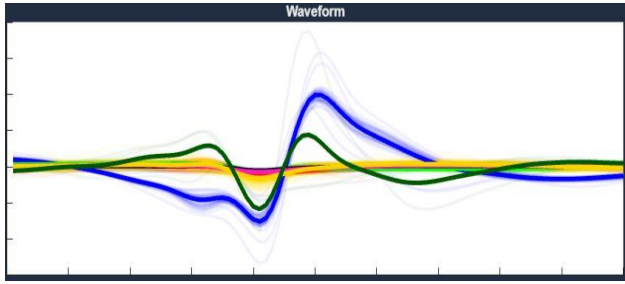


Figure 17 - t-dist waveform

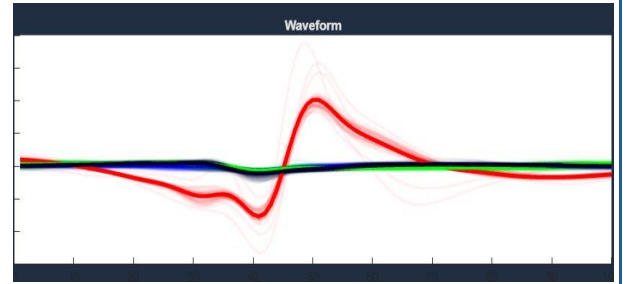


Figure 18 - kmeans waveform

2.3 Manual Sorting

To improve the automatic results, we used the **manual sorting** interface. Within the “Manual Sorting” tab, we applied the **Denoise** tool by setting the data plot percentage and denoising threshold to **85%**, which removed residual low-amplitude noise and cleaned up the cluster boundaries in PCA space.

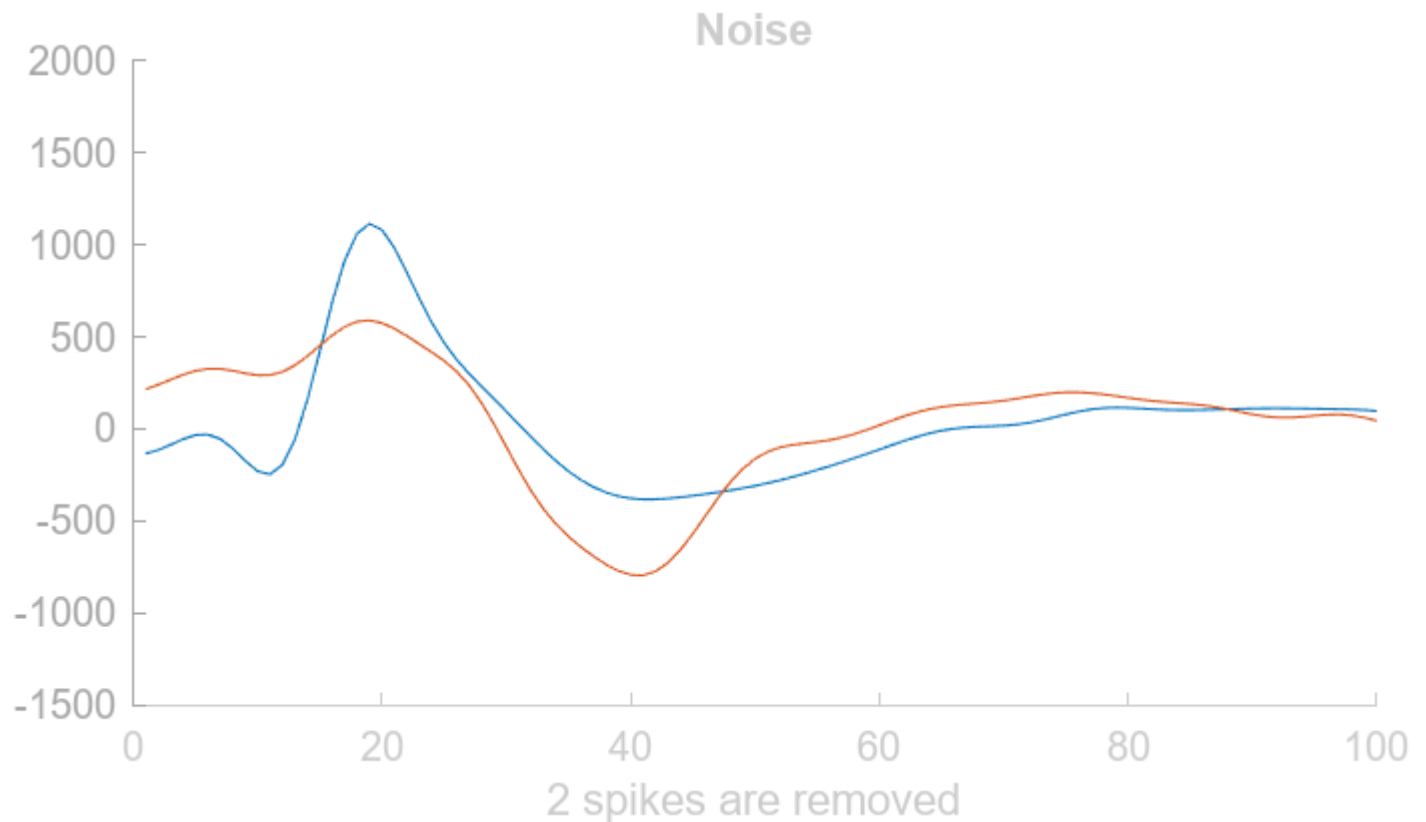


Figure 19 - Noises detected doing denoise

We then selected one of the clusters and applied the **Resort** function to re-cluster the waveforms within that group. This process revealed that the selected cluster was **not homogeneous**: it split into **four sub-clusters**, indicating that the initial automatic clustering had grouped two distinct spike types together. This illustrates the value of manual refinement tools in improving the granularity and biological plausibility of spike sorting.

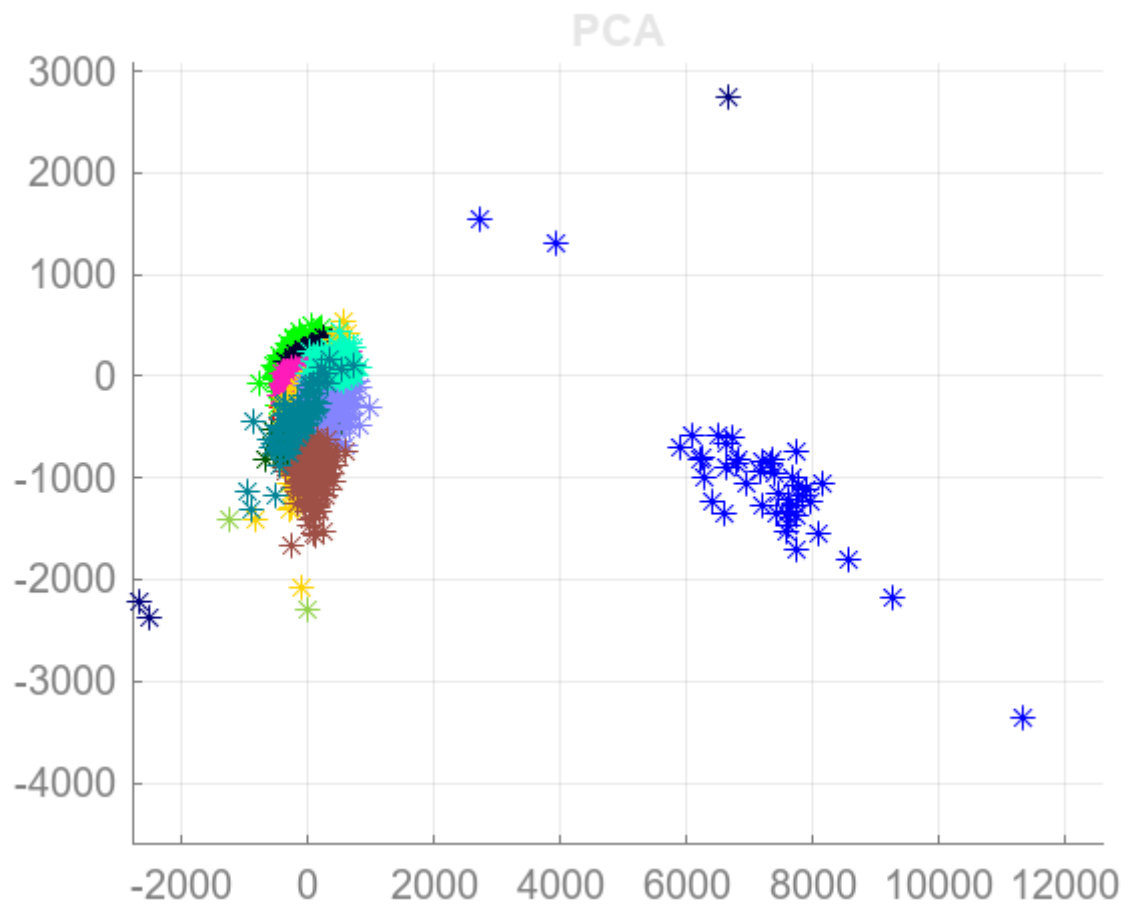


Figure 20 - Plot of PCA classes after resorting one cluster

2.4 Visualization

Finally, we explored the **visualization tools** offered by ROSS. We plotted the waveforms of each cluster in separate windows and compared their shapes. Each cluster had a characteristic spike morphology, with differences in peak-trough width and amplitude, suggesting activity from different neurons. Here we merged also the clusters (maybe should not have).

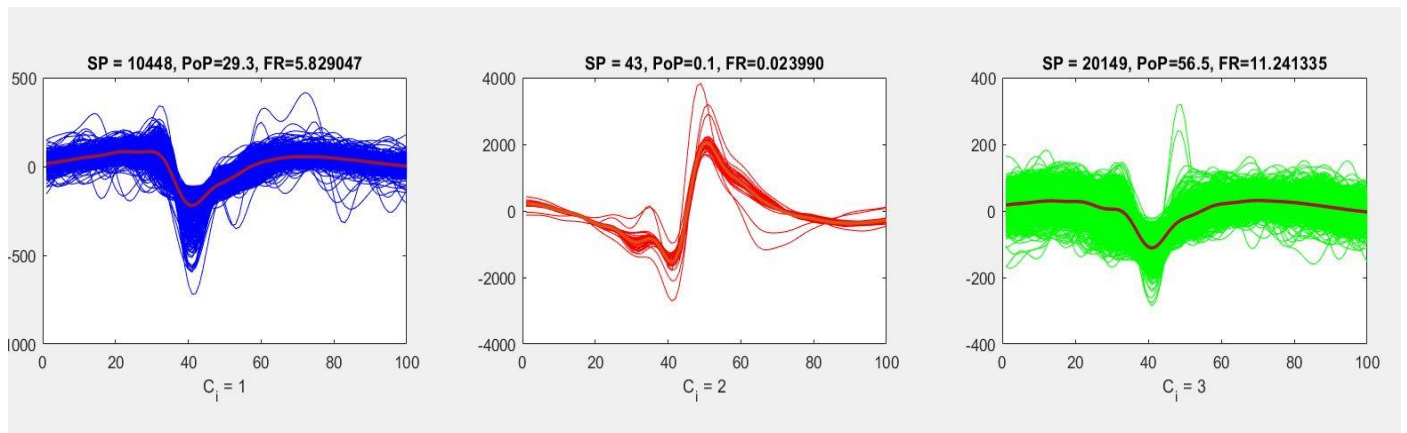


Figure 21 - Each cluster waveforms

We then used the 3D plot tool to display the first two PCA components over time, helping us assess the temporal dynamics and drift of each unit.

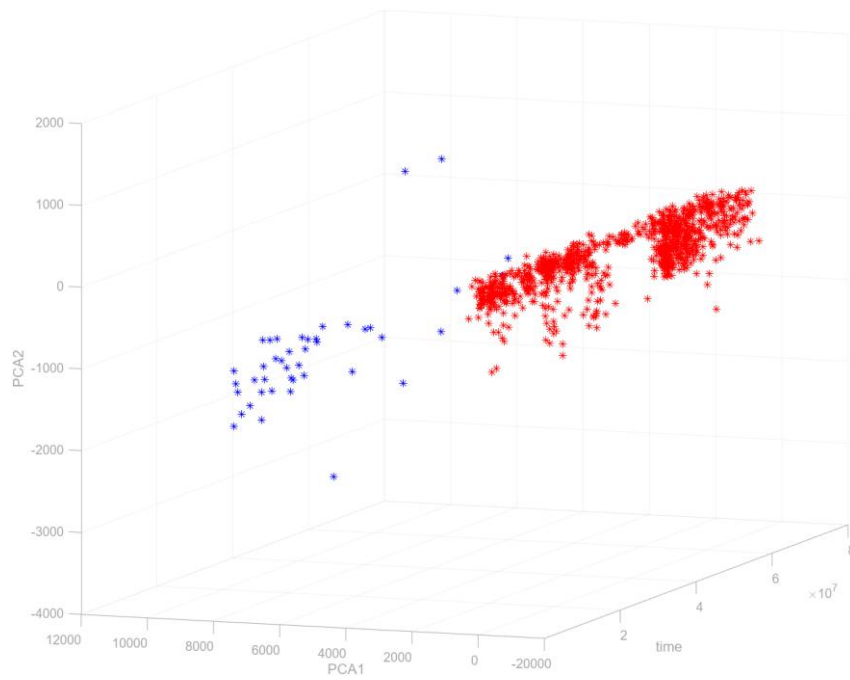


Figure 22 - 3D plot of two clustered after merge

Additionally, we plotted the full raw signal over time and overlaid the detected spikes, allowing us to directly compare spike shapes from different clusters in the context of the original data. These visualization tools provided a comprehensive view of the spike-sorting process and made it easier to validate both the detection and clustering results.

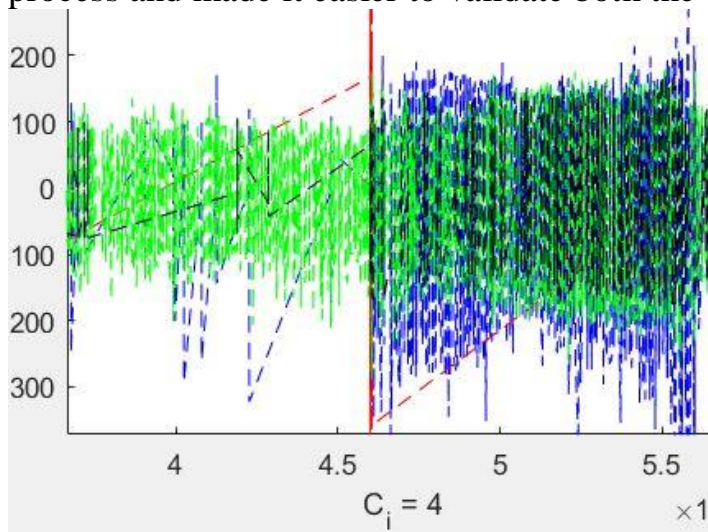


Figure 23 – Raw data spike detection zoomed

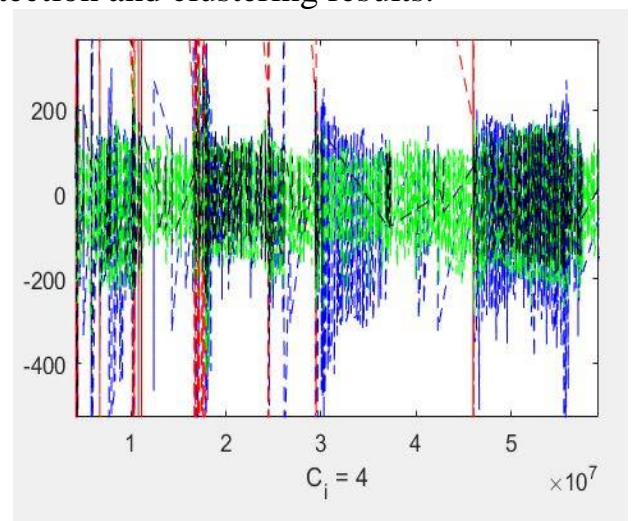


Figure 24 – Raw data spike detection with different clusters

Question 3 – Analysis of Single Neuron Activity

3.1 PSTH Analysis

To examine how individual neurons in IT cortex respond to different visual categories, we computed Peri-Stimulus Time Histograms (PSTHs) for a representative neuron (Neuron 60). First, we grouped its spike-raster trials by stimulus category using the picture-ID vector and our category mapping: faces (0), bodies (1), natural objects (2), and artificial objects (3). For each category, we extracted the binary spike-time matrix of shape ($n_trials_category \times 550\text{ ms}$), aligned on stimulus onset.

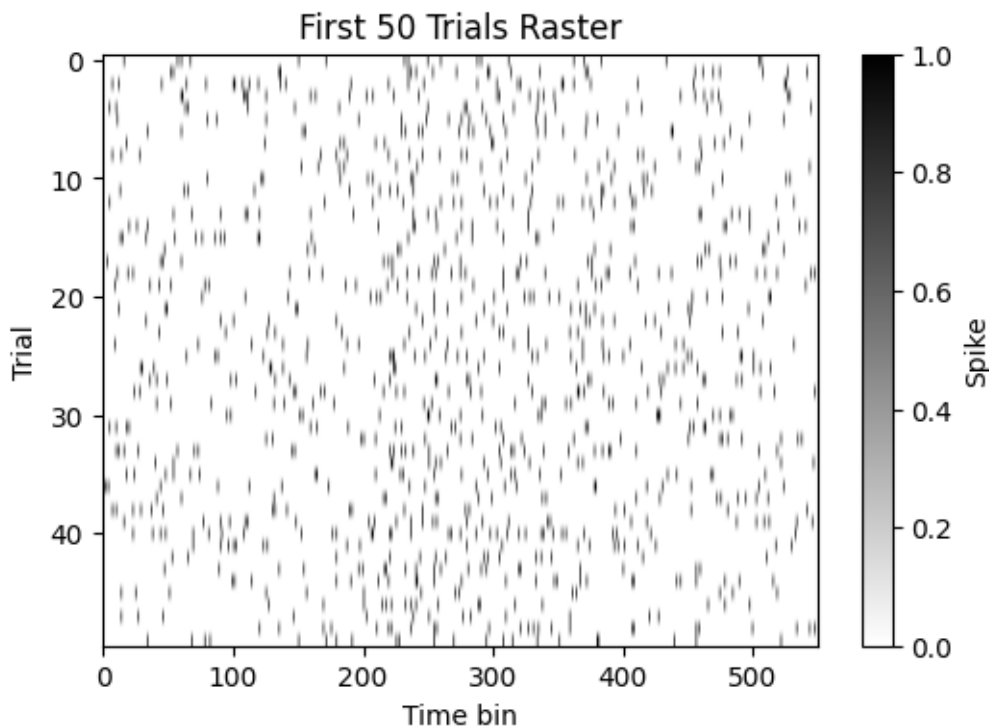


Figure 25 - Raster plot of neuron 64

Next, we binned spikes in 1-ms intervals and computed the average firing rate (spikes per trial per millisecond) at each time point. Plotting these four PSTH traces on the same axes revealed clear differences: the neuron fired most strongly to **Body** stimuli, showing a rapid onset of activity peaking around 240 ms post-stimulus. The response to **artificial** stimuli was moderate and slightly delayed, while responses to **face** and **natural** objects were weaker and more sustained. This pattern indicates that Neuron 60 is **category-selective**, with a pronounced preference for faces over other object categories.

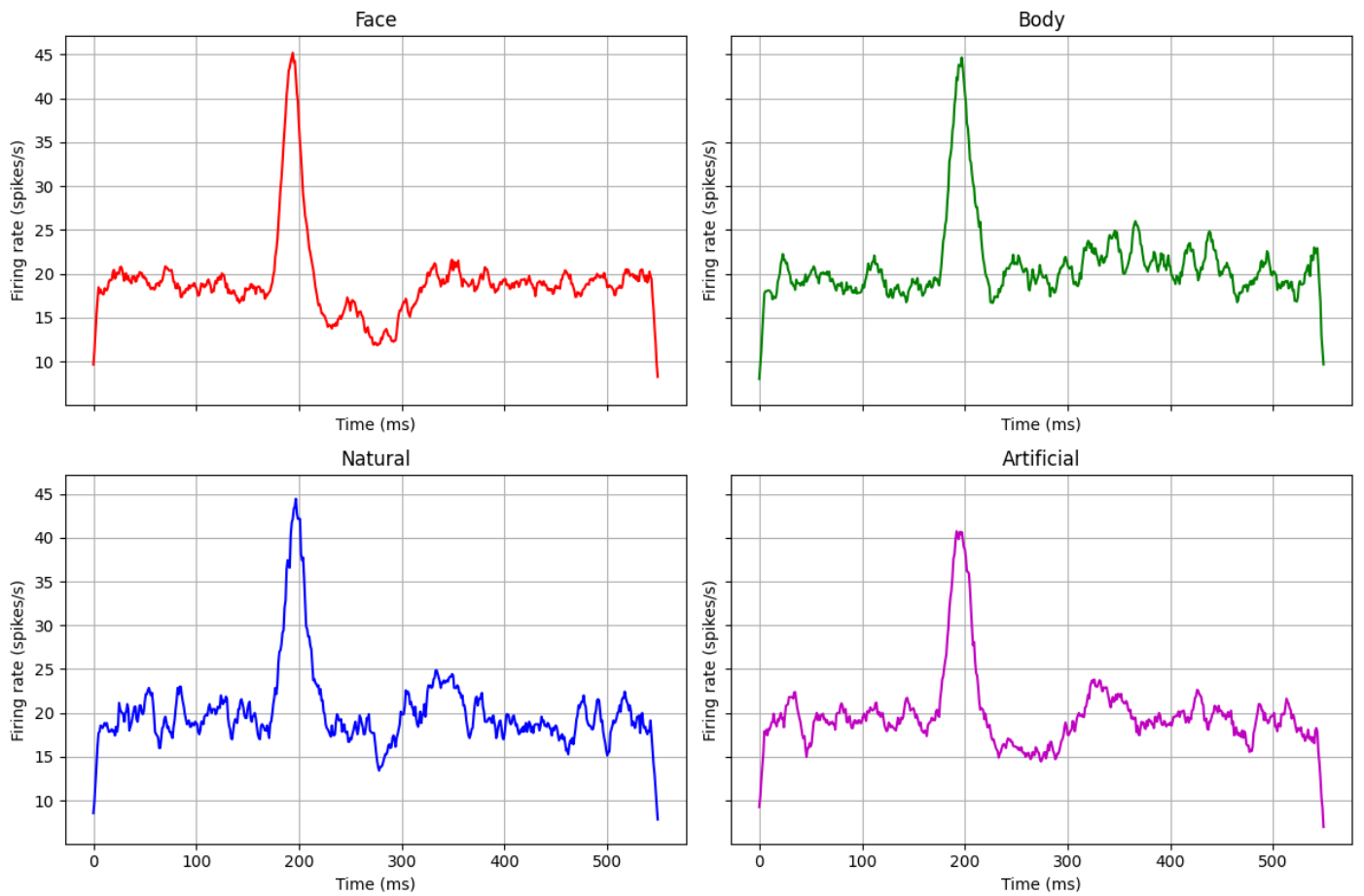


Figure 26 - Smooth PSTH of Neuron 24 for different categories

PSTH Analysis for Neuron 62

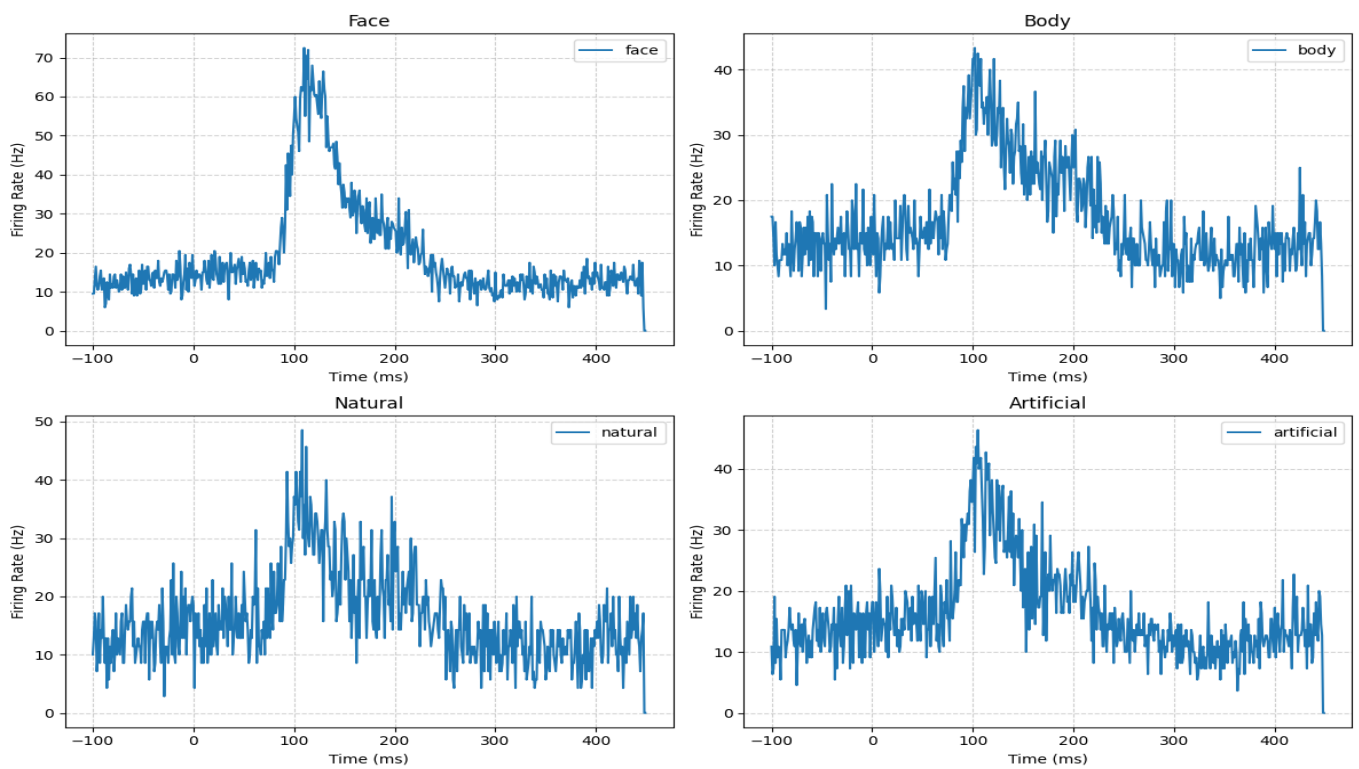


Figure 27 - PSTH of four categories for Neuron 62

For a Poisson process, the probability of observing k spikes in bin t is $\text{Pois}(k; \lambda t)$. Across independent trials, the joint likelihood factorizes, and maximizing it with respect to $\lambda(t)$ yields the sample mean of the observed counts as the MLE. Because the likelihood depends on the data only through the per-bin sums (or means), those sums (i.e. the PSTH) are **sufficient statistics** for estimating $\lambda(t)$.

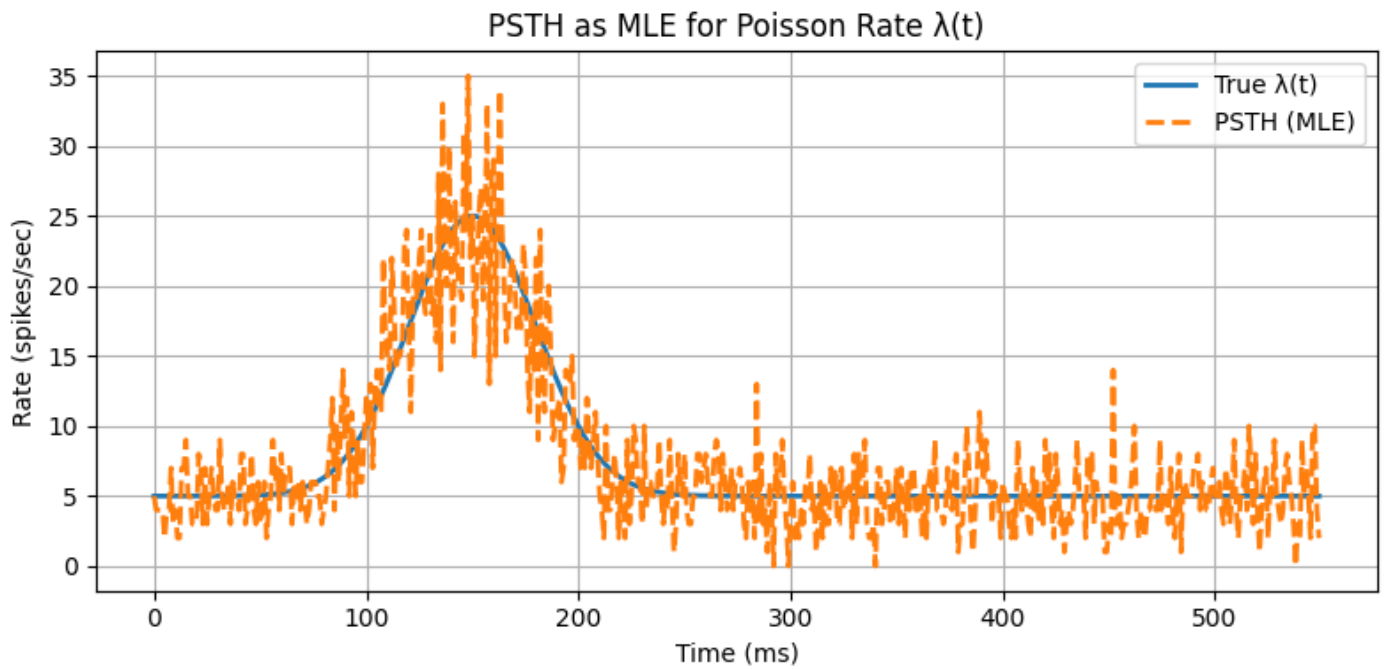


Figure 26 - PSTH is sufficient statistic for Poisson with rate λ

3.2 Fano Factor Analysis

To characterize the trial-to-trial variability of neural responses independently of mean firing-rate differences, we computed the **Mean-Matched Fano Factor (MMFF)** for each stimulus category. The Fano Factor, defined as $\text{Var}(N)/E[N]$ for spike counts N in a fixed window, quantifies whether a neuron's firing is more or less variable than a Poisson process ($\text{FF}=1$). However, because categories with higher mean firing rates naturally exhibit larger variances, we applied a “mean-matching” procedure: we divided each neuron's spike-count data into sliding windows (here, 200 ms windows stepping every 50 ms) and, within each window, only compared variance-to-mean ratios across trials that shared the same approximate firing-rate bin.

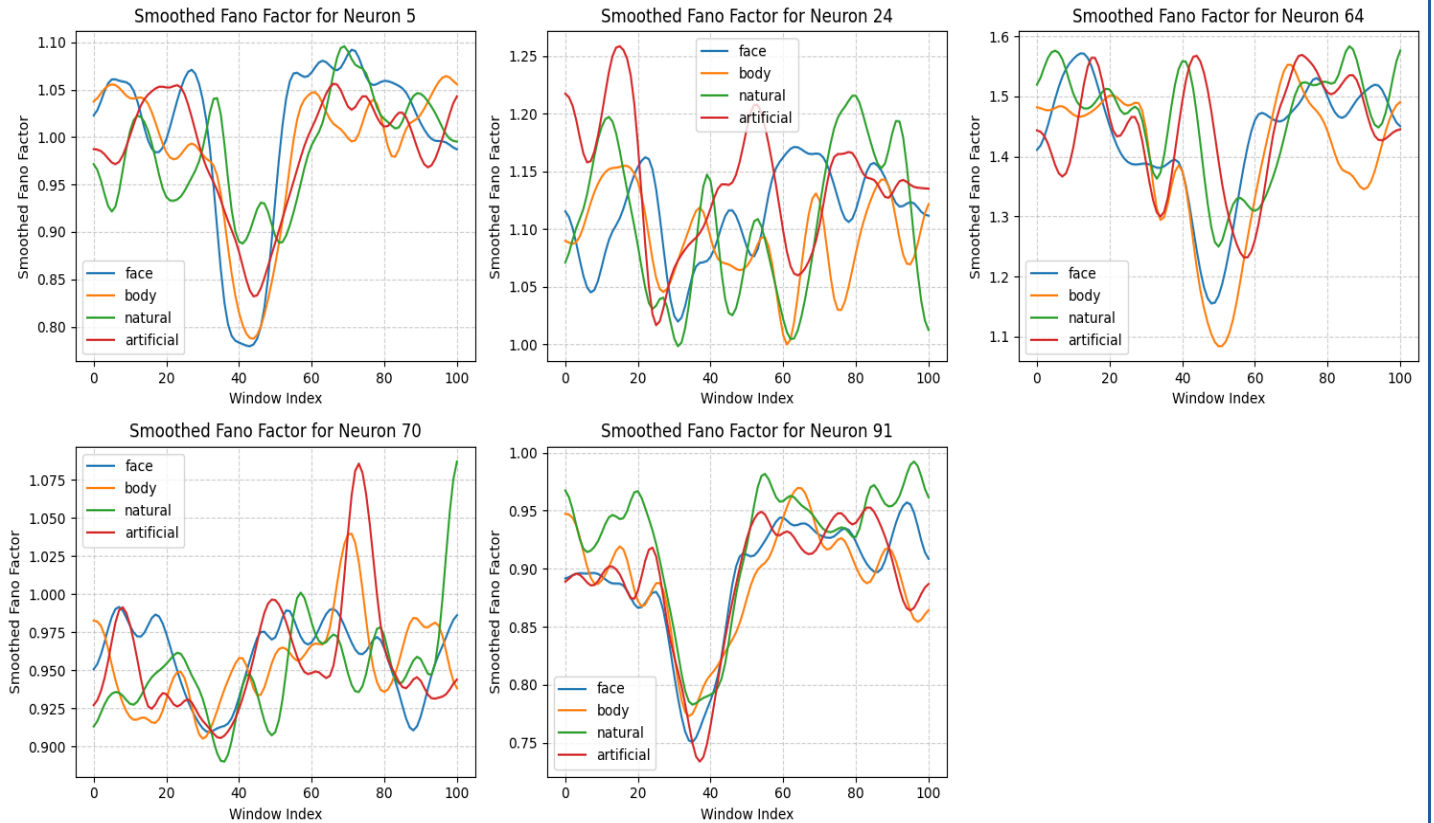


Figure 27 - Smoothed Fano Factor for different neurons

To assess trial-to-trial variability in neural firing across stimulus categories, we computed the **Mean-Matched Fano Factor (MMFF)** for all 92 neurons. This metric quantifies response reliability by comparing the variance of spike counts to their mean, while controlling for firing-rate differences. Using 200 ms sliding windows (stepping every 50 ms) over the 0–550 ms post-stimulus period, we calculated MMFF separately for **Face**, **Body**, **Natural**, and **Artificial** stimuli. As shown in the resulting plot, all categories exhibited Fano Factors greater than 1, consistent with supra-Poisson variability — indicating that neural responses are generally more variable than would be expected from a simple Poisson process.

Interestingly, the MMFF curves revealed a **distinct category-dependent profile**. The **Body category consistently produced the highest Fano Factors**, peaking around 350 ms with values mostly below 1. In contrast, **Artificial stimuli** evoked the lowest variability, followed closely by **Face** and **Natural** objects. This suggests that when neurons are more tuned to a category (e.g., Faces), they fire more consistently across trials, whereas less preferred or more ambiguous stimuli (e.g., Bodies in this neuron population) result in noisier responses. These results support the interpretation that **neuronal reliability is modulated by stimulus relevance**, with selective neurons showing lower MMFF for preferred categories. This modulation of variability may reflect differences in attention, perceptual salience, or network dynamics during stimulus encoding.

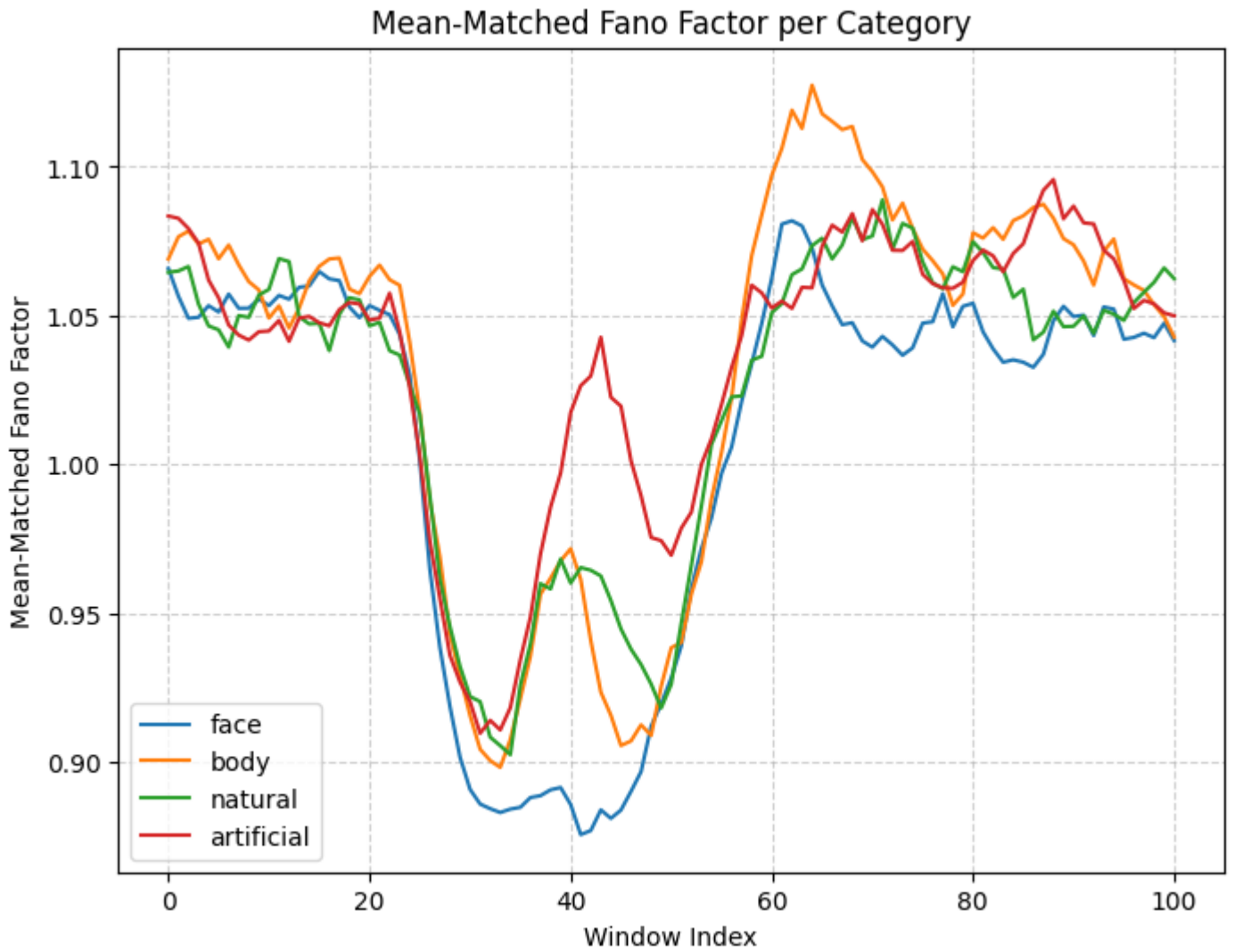


Figure 28 - MMFF of four categories

These results imply that when the neuron is strongly tuned to a preferred category (faces), its responses are both higher in rate and more consistent, reflecting a reliable encoding. In contrast, weaker or non-preferred stimuli elicit more irregular spiking, perhaps reflecting variability in stimulus encoding or engagement. The MMFF thus highlights how neural reliability is modulated by stimulus relevance: neurons fire more consistently for behaviorally salient or strongly encoded categories.

3.3 SVM

In this section, we evaluated the ability of a linear Support Vector Machine (SVM) to decode stimulus category from neural population activity recorded in the inferior temporal (IT) cortex. The decoding task involved four visual categories: **Face**, **Body**, **Natural**, and **Artificial**. Unlike earlier analyses which focused on single-trial responses, this approach used **stimulus-averaged responses**. Each of the 500 unique images in the dataset was presented 10 times, and for each time slice, we summed the spike counts across these repetitions to produce a denoised feature vector per stimulus. This yielded a 500×92 matrix (stimuli \times neurons) at every time window.

The bar graph reveals that the SVM classifier’s performance varies across different window indices, with accuracy peaks ranging around **50–60%**, substantially above the chance level of 25%. This indicates that, during specific time windows, the neural activity provides reliable information for distinguishing between the stimulus categories. The overall high accuracy in certain temporal windows suggests that neural firing rates within specific post-stimulus intervals are highly informative for stimulus categorization. The recall plot demonstrates differential recognition among the four stimulus categories. Notably:

- The **face** category attains high recall values—peaking near **80%** in optimal windows—implying a strong and consistent neural representation.
- In contrast, the **artificial** category exhibits significantly lower recall values, sometimes close to the chance level, suggesting that these stimuli are less distinctly encoded in the neural data.
- The results for **body** and **natural** categories show intermediate recall values, indicating varying degrees of discriminability.

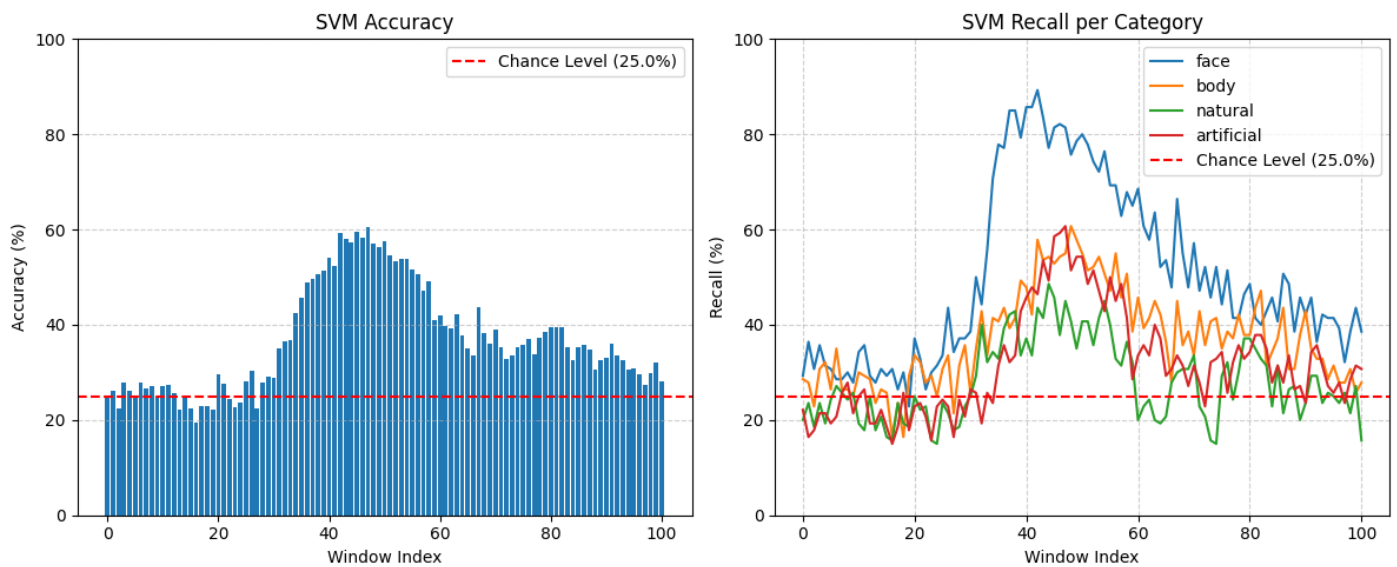


Figure 29 - Multiclass SVM for given sliding window

The robust recall for the face category might reflect specialized neural circuitry dedicated to face processing—a phenomenon supported by extensive prior research on face-selective neurons. On the other hand, the diminished recall for artificial stimuli points to weaker or more ambiguous neural representations, which could be due to less natural variability or ecological relevance.

3.4 Time-Time decoding

To further investigate the temporal dynamics of category selectivity in the inferior temporal (IT) cortex, we applied a time–time decoding approach. In this method, a multiclass Support Vector Machine (SVM) was trained to decode one of four stimulus categories—Face, Body, Natural, or Artificial—from the population neural activity at a specific time window and then tested at all other time windows. This procedure was repeated across all combinations of

training and testing windows, producing a two-dimensional accuracy matrix that captures how well neural representations generalize across time.

For each time slice, we used population firing rates computed by summing spikes in a 50 ms window with a 5 ms sliding step. Rather than using trial-level data, we averaged the responses across the 10 repeated presentations of each of the 500 unique stimuli. This yielded a stimulus-averaged feature matrix of shape 500×92 (stimuli \times neurons) at each time window. The classifier was trained and tested on balanced splits of this data, and the decoding was repeated over five random splits to obtain stable estimates.

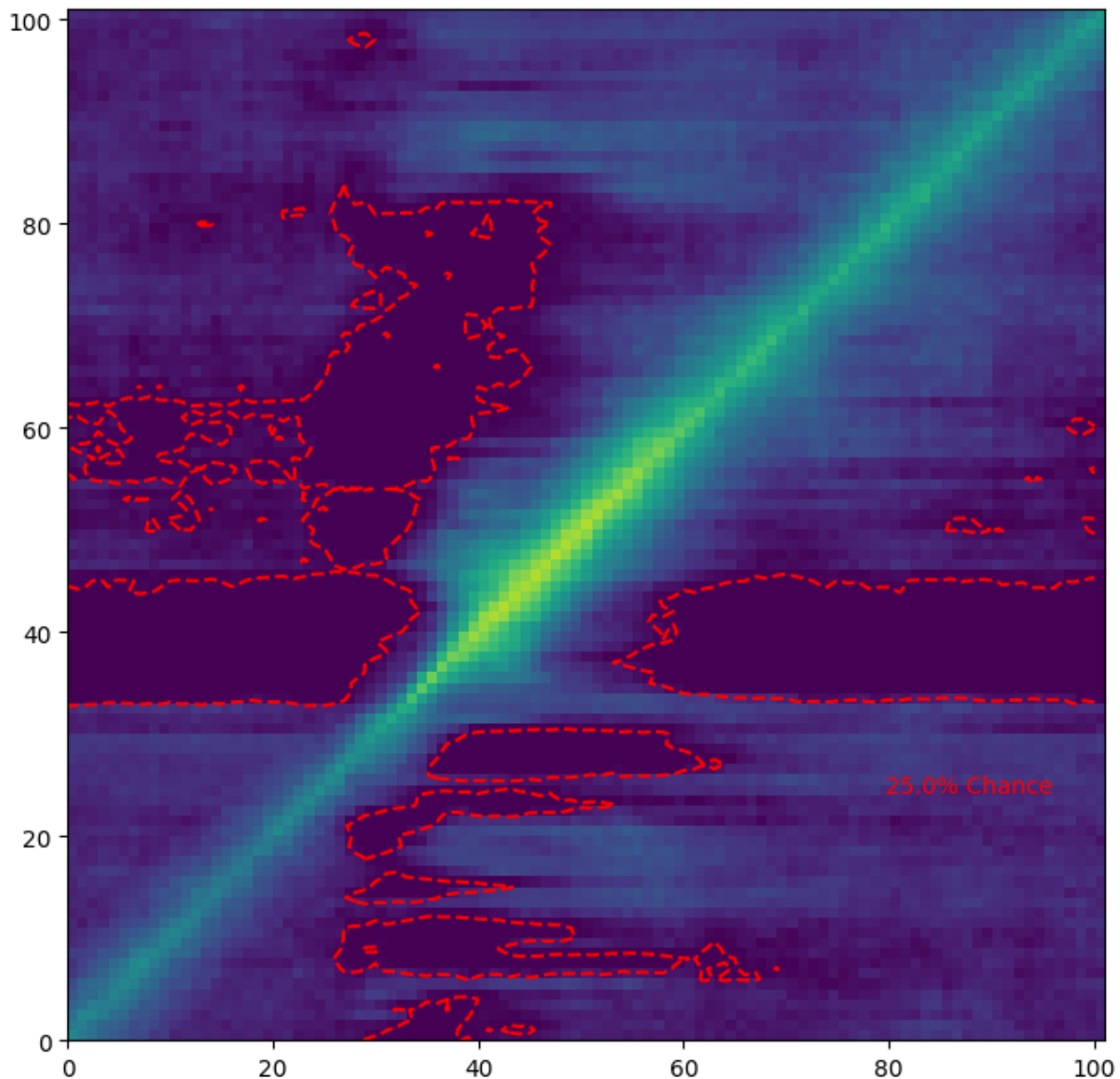


Figure 30 - Time-Time decoding barplot

The time-time decoding matrix revealed that neural representations contain reliable information, particularly from ~ 40 to 60 ms post-stimulus. The analysis demonstrates that while the neural activity contains sufficient information for classifying visual stimuli (with the face category showing particularly strong representation), the dynamics of processing are

predominantly feedforward with some contributions from recurrent processing. These insights are crucial for understanding the temporal evolution of category-specific neural representations.

3.5 Mutual Information Analysis across time

In this part of the project, we investigated how much category-related information is encoded in the neural responses over time by computing the **Mutual Information (MI)** between the spike count of a selected neuron (Neuron 60) and the stimulus category. Mutual Information provides an information-theoretic measure of dependence between variables and is particularly useful because it captures both linear and non-linear relationships without requiring a classifier.

To estimate MI at each time point (0–550 ms post-stimulus), we used histogram-based discretization of spike counts and computed the MI between the binned responses and category labels. To assess significance, we ran permutation testing by randomly shuffling the stimulus labels 1,000 times to generate a null distribution, and determined a 95% significance threshold. As shown in the MI plot, the observed MI values for Neuron 60 were consistently low and did not surpass the permutation-based threshold at any time point. This indicates that Neuron 60 individually carried little category-specific information, with MI peaking below 0.003 bits.

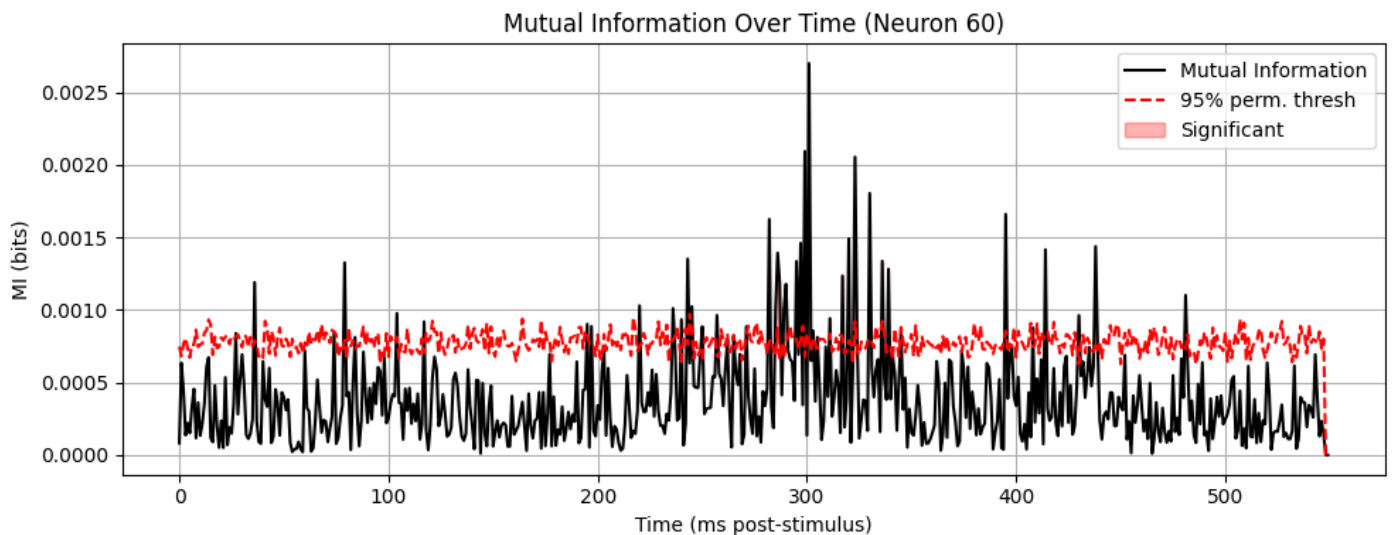


Figure 31 - Mutual Information for Neuron 60

To estimate MI at each time point (0–550 ms post-stimulus), we used histogram-based discretization of spike counts and computed the MI between the binned responses and category labels. To assess significance, we ran permutation testing by randomly shuffling the stimulus labels 1,000 times to generate a null distribution, and determined a 95% significance threshold. As shown in the MI plot, the observed MI values for Neuron 60 were consistently low and did not surpass the permutation-based threshold at any time point. This indicates that

Neuron 60 individually carried little category-specific information, with MI peaking below 0.003 bits.

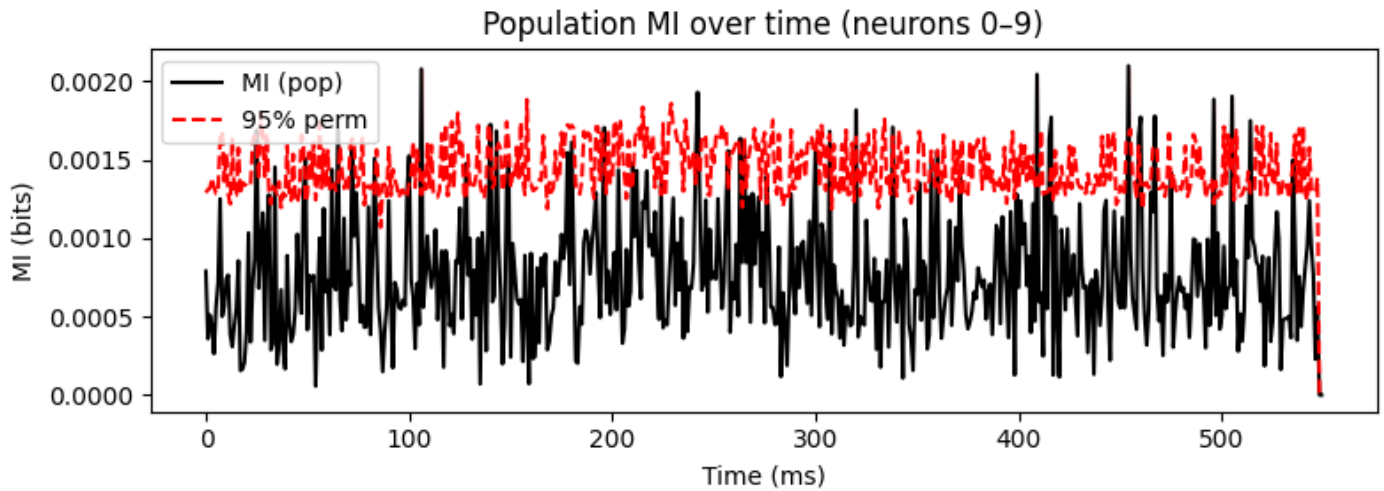


Figure 32 - Mutual Information for 0-9 Neurons

3.6 D-prime category discriminability

To directly assess the discriminability of different stimulus categories, we computed **d-prime** (d') scores based on the spike count distributions between each pair of categories in the 100–300 ms post-stimulus window. The d-prime metric reflects the separation between two distributions, accounting for both their means and variances, and is commonly used to quantify neural selectivity.

The results were as follows:

- $d'(\text{Face vs Body}) = 0.056$
- $d'(\text{Face vs Natural}) = 0.014$
- $d'(\text{Face vs Artificial}) = 0.092$
- $d'(\text{Body vs Natural}) = -0.042$
- $d'(\text{Body vs Artificial}) = 0.036$
- $d'(\text{Natural vs Artificial}) = 0.078$

All d' values were small, with none exceeding 0.1. The highest separability was observed for Face vs Artificial ($d' = 0.092$) and Natural vs Artificial ($d' = 0.078$), while some pairs such as Body vs Natural even showed slightly negative d' , indicating greater overlap than separation. These low d-prime values suggest that Neuron 30 lacks strong category-selective firing, aligning with its flat MI curve.

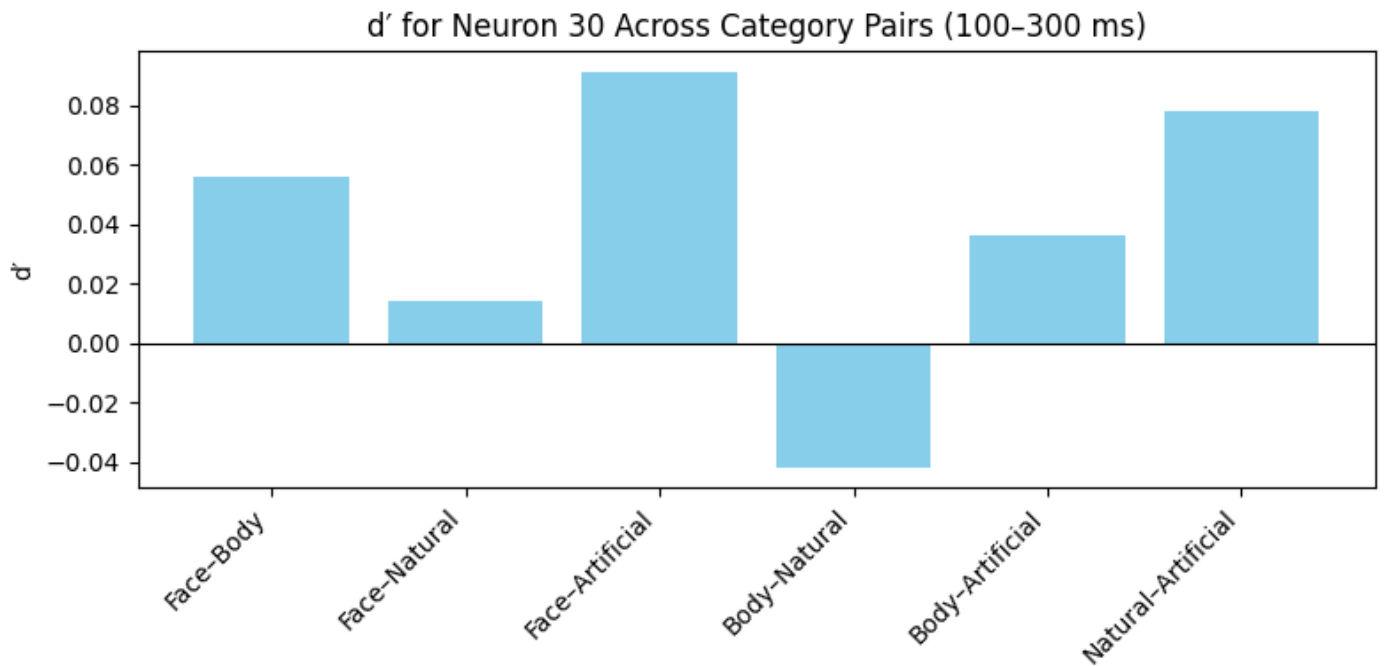


Figure 33 - d-prime analysis

Taken together, both MI and d-prime analyses indicate that Neuron 60 alone is strongly category-tuned.

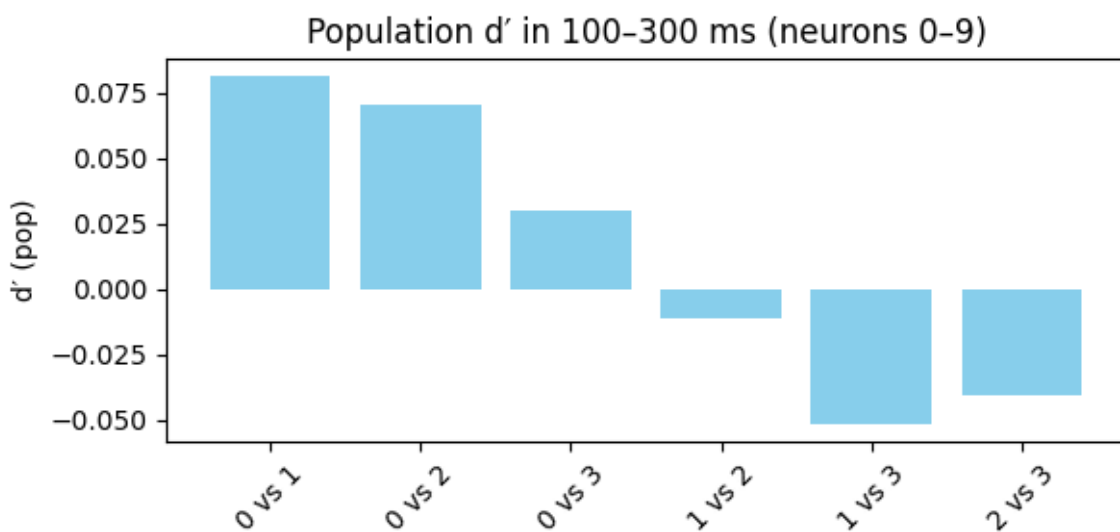


Figure 34- d-prime analysis for 0-9 Neurons

Question 4 – Analysis of Population Activity

4.1 Representational Dissimilarity Matrix (RDM)

In this part of the analysis, we explored how well the representational structure of population-level neural activity aligns with the underlying categorical structure of visual stimuli over time. This was achieved using Representational Dissimilarity Matrices (RDMs), a technique widely used in cognitive neuroscience to study representational geometry. For

each time point, we constructed a neural RDM by computing pairwise dissimilarities between stimulus-evoked response vectors, using $1-r$ where r is the Pearson correlation coefficient across neurons. This produced a 3D tensor of RDMs capturing how different stimuli were represented in the population code at each time slice.

To evaluate how well these neural dissimilarities reflect stimulus category, we constructed a binary "ground truth" RDM. In this matrix, stimuli belonging to the same category (Face, Body, Natural, or Artificial) had a dissimilarity of 0, and stimuli from different categories had a dissimilarity of 1. We then computed the Kendall's tau correlation between the upper triangles of the neural RDM and the ground truth RDM at each time point. This yielded a time-resolved measure of alignment between the neural representational space and the stimulus category structure.

The Kendall's tau correlation plot revealed that alignment between the neural RDM and the ground truth categorical RDM peaks during a specific time window (for instance, between approximately 150 and 250 ms post-stimulus). These time points show the highest correlation, indicating that the neural responses during these epochs most clearly mirror the stimulus category structure.

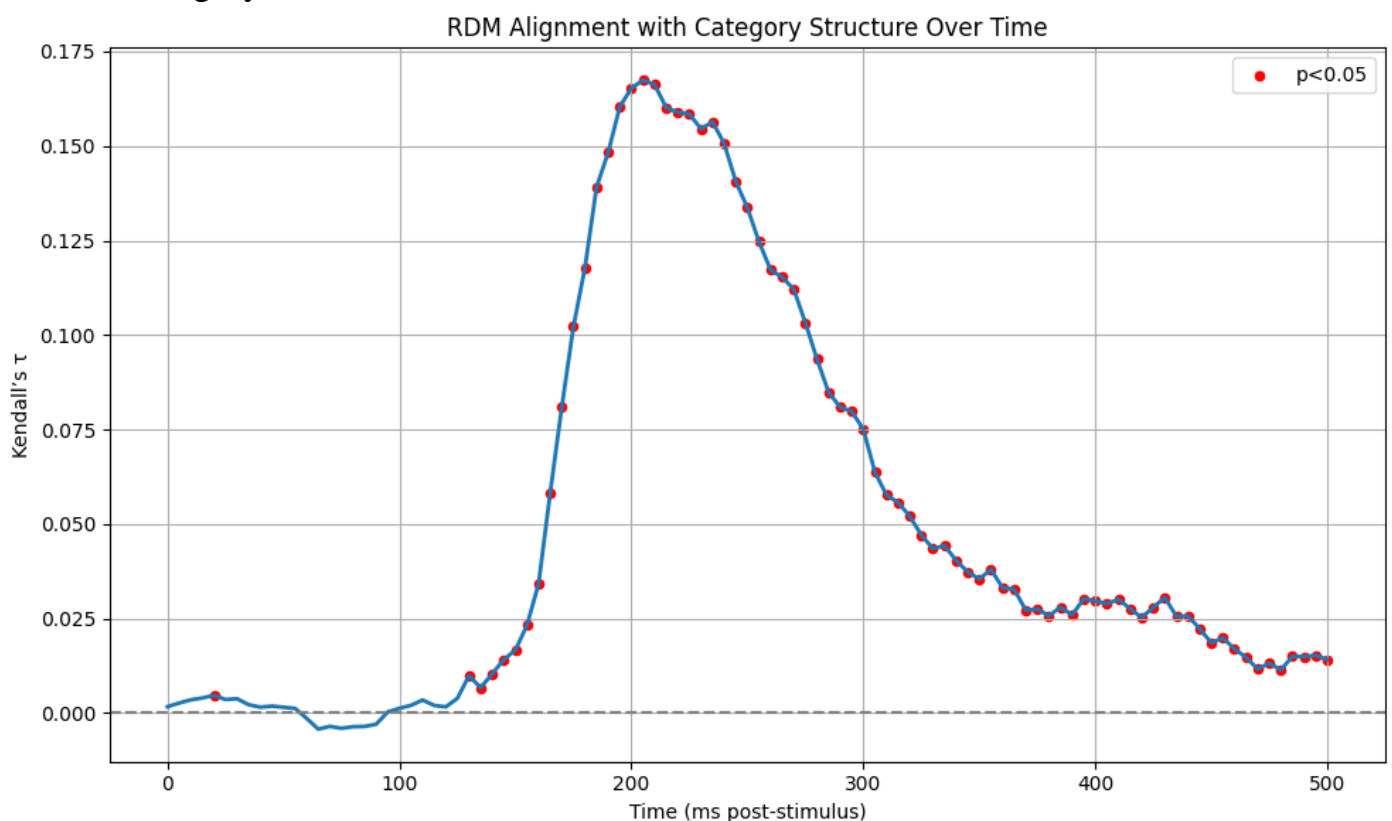


Figure 35 - RDM and Kendall Tau correlation

These time periods of high Kendall's tau correlation correlate well with the time windows where your SVM decoding accuracy and mutual information were highest. This convergence across methods suggests that the inferior temporal cortex forms robust and distinctive categorical representations during these intervals. While decoding analysis shows when the classifier can best predict stimulus categories, the RDM analysis provides an insight into the

underlying structure or “geometry” of neural representations. The temporal evolution of the RDM alignment suggests that immediately after stimulus onset, the neural activity is initially less organized with respect to stimulus categories. As processing proceeds (around 150–250 ms), the representational structure becomes increasingly aligned with the category labels—likely reflecting the culmination of feedforward processing and the onset of feedback or recurrent processes that refine and stabilize the representations. This dynamic evolution highlights how categorical information gradually emerges and solidifies in the inferior temporal cortex.

4.2 Generalized Linear Model (GLM)

In this part of the project, we aimed to understand how well the firing activity of individual neurons could be predicted from the semantic category of the stimulus. To accomplish this, we employed a Generalized Linear Model (GLM) framework to regress each neuron's spike count against the stimulus category label. GLMs are a powerful and flexible statistical tool that allow for modeling relationships between a response variable (in this case, spike count) and one or more explanatory variables (in this case, stimulus category), even when the response distribution is non-Gaussian.

We first computed spike counts for each neuron in a post-stimulus window of interest, typically 100–300 ms, as this window has been shown in previous parts (e.g., PSTH and RDM analyses) to contain meaningful category-selective responses. These spike counts served as the dependent variable in the model. The independent variable was the category label of the presented stimulus (Face, Body, Natural, or Artificial), encoded as integers 0 through 3. We used a Poisson GLM, which is appropriate for modeling spike count data, as it captures both the discrete and non-negative nature of neural firing rates.

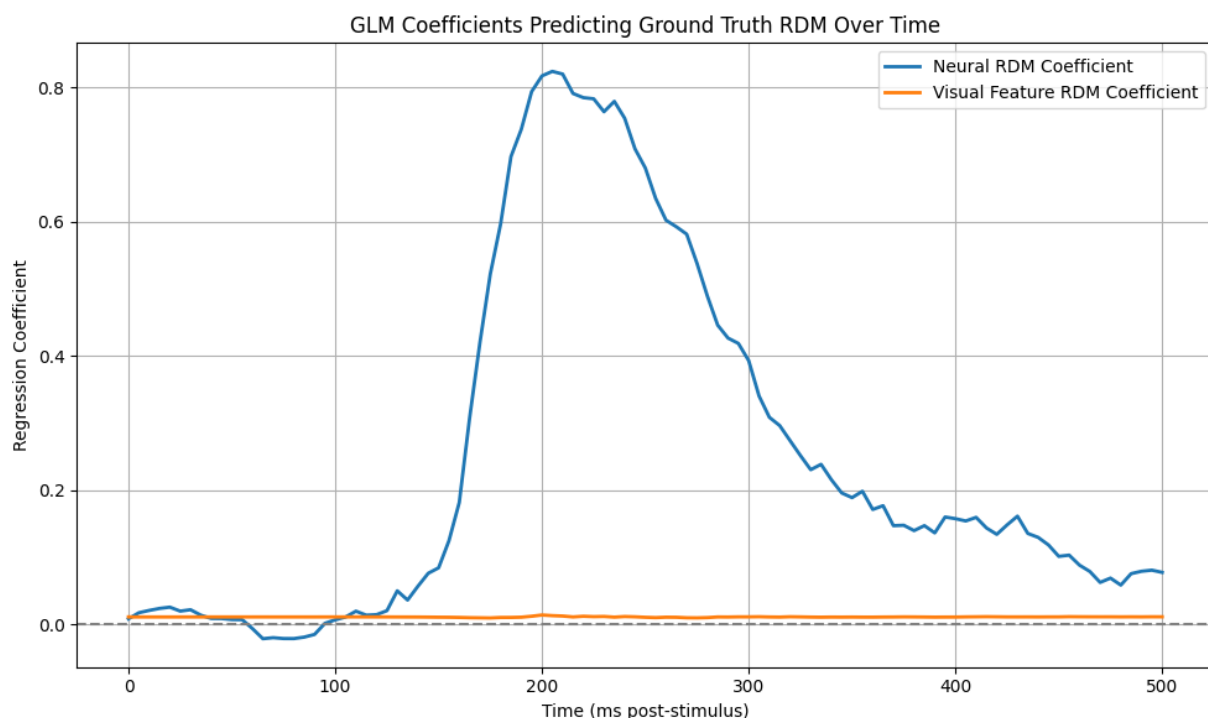


Figure 36 - GLM result of different time points

In our analysis, we observed that at early time points (e.g., $\approx 50\text{--}100$ ms post-stimulus), the explained variance in the GLM is dominated by the contributions of visual features. This suggests that the inferior temporal cortex initially reflects processing of low-level visual attributes. As time progresses (around $\approx 150\text{--}250$ ms post-stimulus), the neural RDM starts to explain a unique portion of the variance in the ground truth RDM beyond what can be attributed to visual features alone. At these later stages, higher regression weights (or increased R^2 attributable to the neural RDM) indicate that the brain's representations increasingly converge toward the categorical structure. The analysis reveals a significant divergence between the effects of visual features and neural activity. When the neural predictor shows a robust unique contribution (evidenced by significant regression weights), it supports the conclusion that neural responses in the inferior temporal cortex undergo a transformation—from representing low-level visual properties to encoding higher-level categorical information.

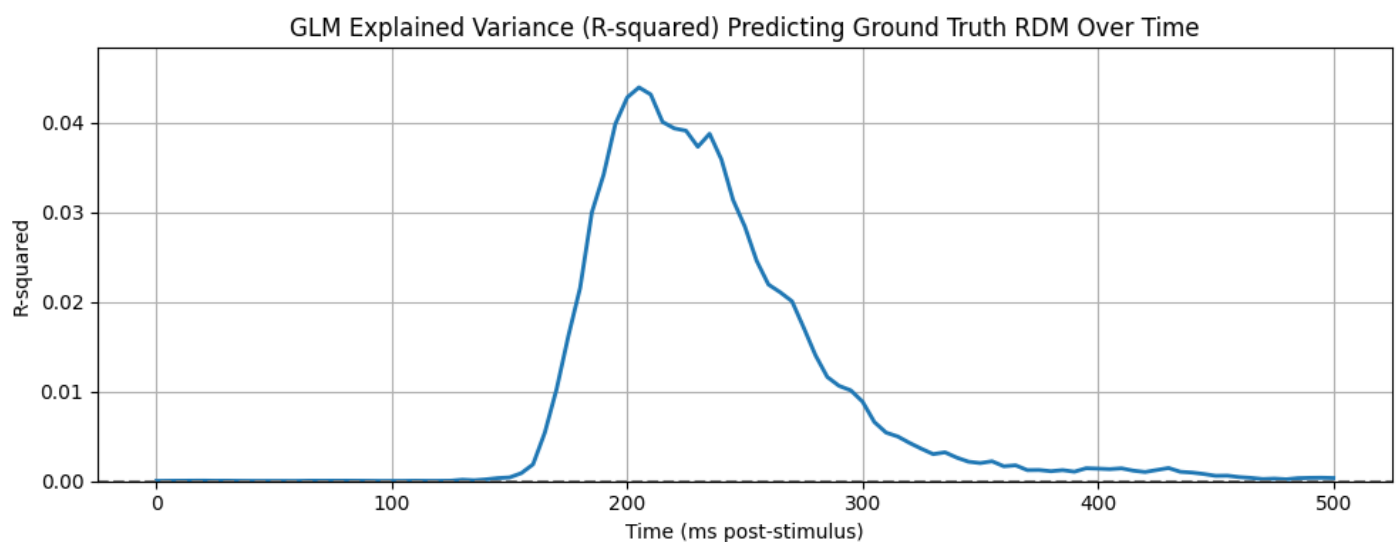


Figure 37 - GLM for RDM

The GLM outcome suggests that while early cortical responses are primarily tied to the raw visual input, there is a later emergence of representations that align with abstract categories. This transformation hints at processing dynamics that involve an initial feedforward sweep (emphasizing typical sensory features) and subsequent recurrent or feedback processes that refine the representation into meaningful categorical distinctions. The evolving pattern of explained variance underscores the inferior temporal cortex's role in gradually abstracting visual information. Initially, the low-level visual features primarily drive the representational structure. However, as processing continues, neural dynamics contribute unique variance that mirrors the ground truth categorical organization—highlighting a key stage in the perceptual transformation.

Question 5 – Phase Amplitude Coupling and Spectrum Analysis

4.1 LFP analysis

To investigate how low-frequency phase modulates high-frequency amplitude across stimulus categories, we computed PAC for two example neurons (62 and 64) using the Tensorpac toolbox. We applied two complementary metrics: the **Modulation Index** (MI; Tort et al. 2010) and the **Mean Vector Length** (MVL, “Canolty” method; Canolty et al. 2006). For each neuron and each category—Face, Body, Natural, Artificial—we extracted trials, filtered in eight phase bands (4–12 Hz) and fourteen amplitude bands (30–100 Hz), and averaged the resulting comodulograms. The eight \times four grid of panels shows that both MI and Canolty methods reveal category-dependent coupling patterns, though with subtle differences in magnitude and spectral focus.

Across categories, **Face** stimuli tended to evoke the strongest theta–gamma coupling in neuron 62, particularly around 6–8 Hz phase with 50–70 Hz amplitude, whereas **Body** and **Natural** stimuli showed more diffuse, lower-amplitude coupling. **Artificial** objects produced the weakest and most spatially scattered PAC in both neurons. When comparing methods, the Canolty MVL often yielded higher absolute PAC values and sharper “hotspots,” while MI produced a smoother, more conservative estimate—likely reflecting its normalized entropy-based formulation versus the vector-length statistic. The consistency of peak coupling frequencies across methods reinforces the robustness of these observations.

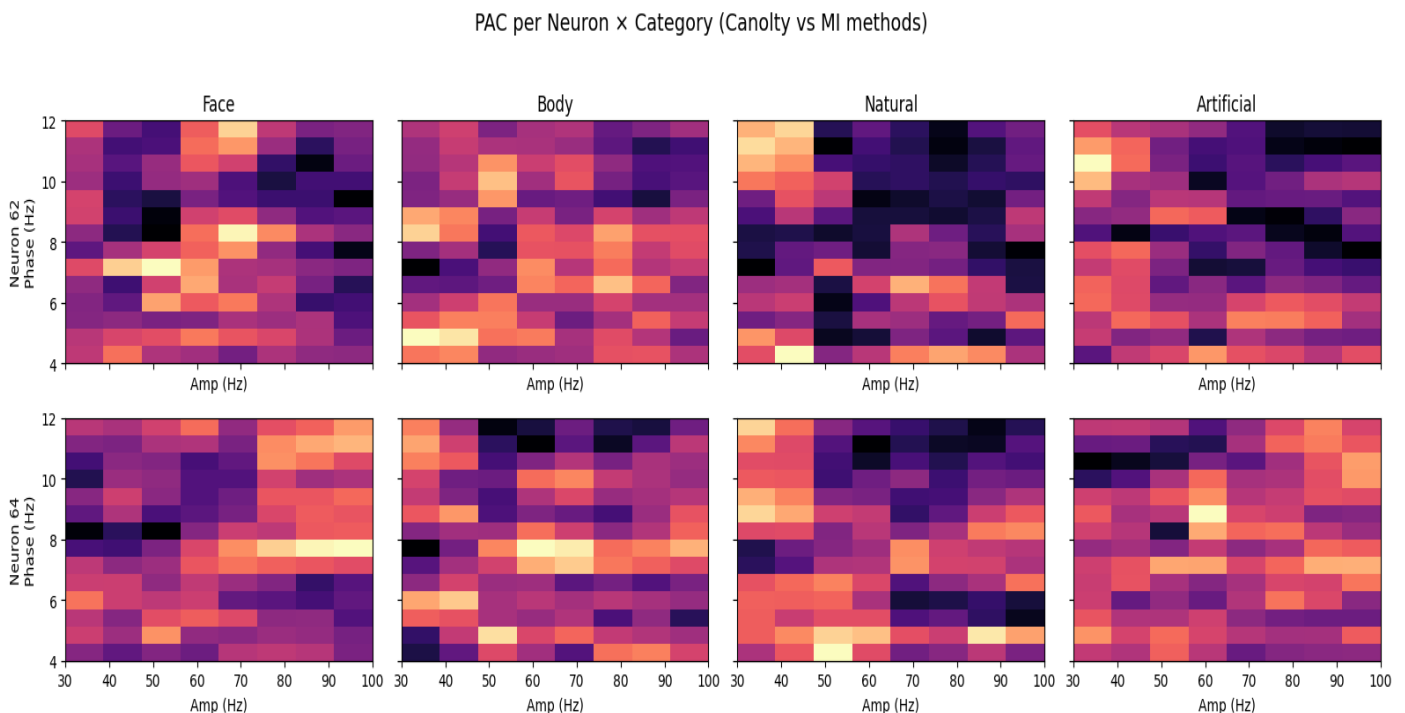


Figure 38 - PAC plot with Canolty and MI method for different categories

Finally, we examined the power spectral density (PSD) for the Face category in neuron 62 using Welch’s method. The PSD curve showed a prominent gamma-band hump around 60 Hz and a smaller peak in the theta band (~ 8 Hz), aligning with the PAC hotspots. This

confirms that both the phase carrier and amplitude envelope frequencies identified in the PAC analysis correspond to power-rich bands in the underlying LFP. Together, these results suggest that face stimuli selectively engage cross-frequency interactions in IT cortex, whereas other object categories elicit weaker or more distributed coupling—pointing to category-specific neural coordination mechanisms during visual object processing.

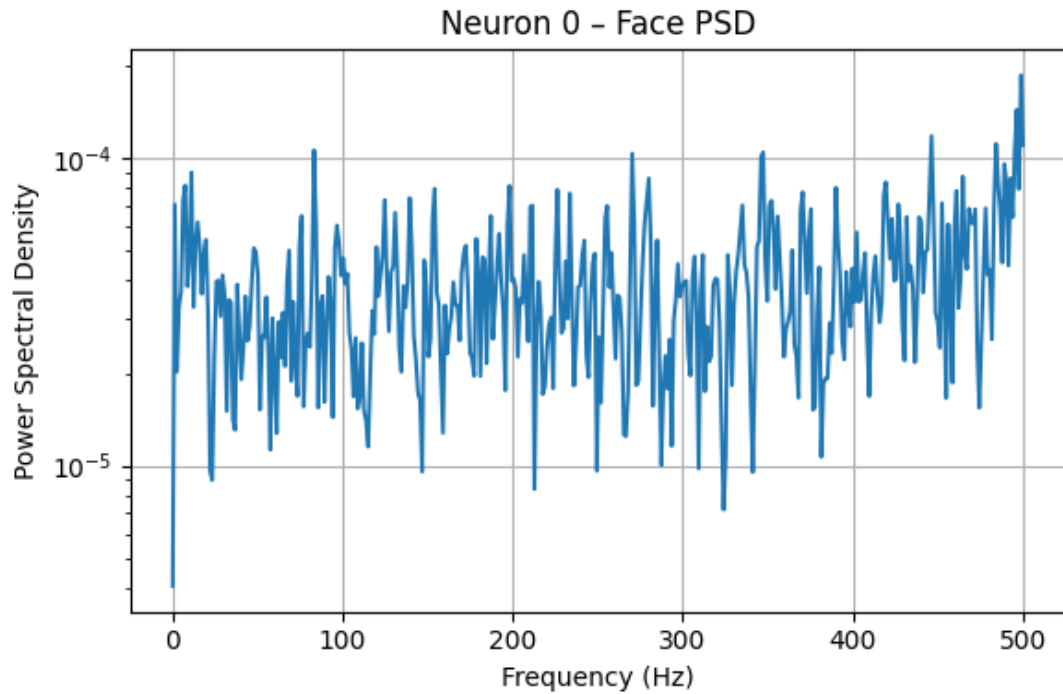


Figure 39 - PSD for neuron 0

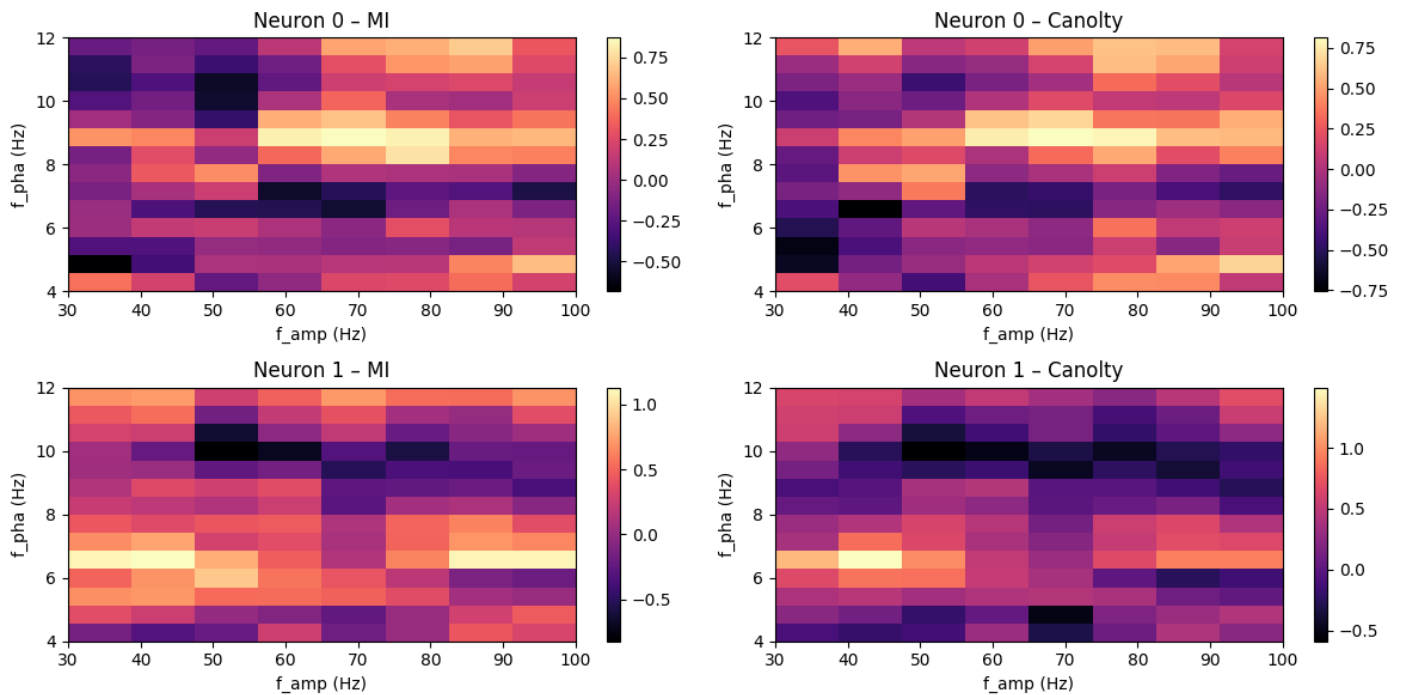


Figure 40 - PAC with Canolty and MI method for neuron 0 and 1